ABSTRACT

LUGO, RAFAEL ANDRES. Methods of Flight Parameter Recovery from Orion Crew Module Using Scale Model Aeroballistic Flight Data. (Under the direction of Robert Tolson & Andre Mazzoleni.)

Data from the inertial measurement unit aboard the Crew Exploration Vehicle Pressure Transducer Model was analyzed and compared to radar and pressure-derived flight parameters. Radar data were validated by comparing Mach number, angle of attack, and sideslip to pressure-derived Mach number and flight angles. Various methods were used to validate the sensor data, including computing angular rates and body accelerations from sources other than the rate gyroscopes and accelerometers. The vehicle trajectory was also reconstructed from the inertial measurement unit data, and compared with pressure-derived trajectory. Comparison of the different trajectory reconstruction methods resulted in significantly higher confidence in the pressure-based solution.

Methods of Flight Parameter Recovery from Orion Crew Module Using Scale Model Aeroballistic Flight Data

by
Rafael Andres Lugo

A thesis submitted to the Graduate Faculty of
North Carolina State University
in partial fulfillment of the
requirements for the Degree of
Master of Science

Aerospace Engineering

Raleigh, North Carolina

2011

APPROVED BY:

_____
Dr. Andre Mazzoleni, Chair of Advisory Committee

_____ _____
Dr. Robert Tolson Dr. Fred DeJarnette

Biography

Rafael Lugo was born on July 18th, 1985 to Gabriel and Ana Maria Lugo in Wilmington, North Carolina. He is the older brother of Miguel Lugo. Having attended Snipes Elementary School, D.C. Virgo Middle School, and New Hanover High School, Rafael was accepted to North Carolina State University in 2003 with two merit-based scholarships. He graduated with a Bachelor of Science degree in aerospace engineering in the spring of 2007, and was subsequently accepted into NC State University's graduate school. He was also accepted into the Graduate Research Assistantship program at National Institute of Aerospace located in Hampton, Virgina. Through this program he was able to work with NASA Langley Research Center's Atmospheric Entry and Flight Systems Branch in conducting his Master's thesis research. He currently resides in Hampton, where is working with NASA-LaRC and NIA in pursuing a doctoral degree in aerospace engineering from NC State University.

Acknowledgements

The methods of analysis presented in this thesis are the result of over two years of investigation. I could not have gotten to this stage without the guidance, knowledge, and inspiration provided by Dr. Robert Tolson. I cannot express in enough words my admiration and awe at his brilliance and gift of intuition. Mark Schoenenberger, of LaRC's Atmospheric Entry and Flight Systems Branch, constantly provided a fresh perspective on my work, and I am indebted to him for his support and guidance. Dr. Andre Mazzoleni's help and advice was, as always, a much-needed source of encouragement. Along with Dr. Mazzoleni, Dr. Fred DeJarnette guided me throughout my undergraduate career and into my graduate career, and I cannot thank them enough. I would of course be remiss in not thanking Thomas Sebastian, whose Master's work I built upon. All of the people I have mentioned here continue to be a source of inspiration for me, and I wish them well in all of their endeavors. I would also like to acknowledge and thank the support of NASA Langley Research Center, the US Army Research Laboratory, and the National Institute of Aerospace.

Finally, I would like to thank my family for their ever-present love and support. They were the calm in the storm that was my research, and they continue to be the loving family that I always look forward coming home to.

Table of Contents

List of Tables

List of Figures

1 Introduction

Over the years, the Return-to-Moon mission proposed by the United States and spearheaded by the National Aeronautics and Space Administration in 2004 has evolved into the Constellation project. Like the Apollo program of the 1960s, the Constellation design consists of advanced launch vehicles, spacecraft, and mission profiles.

As with any scientific and technological endeavor, the theories, techniques, and technologies must be rigorously tested and verified before the astronauts set foot on the spacecraft. Pursuant to this effort, NASA has undertaken the most intensive series of experiments and studies since the Shuttle Transportation System (STS) was devised in the late 1970s. So extensive is this effort, that even the venerable STS is being discontinued to make way for Constellation.

Figure 1.1: Project Constellation

Designed as a successor to Apollo, the Constellation architecture consists primarily of two launch vehicles: the Ares I and Ares V. Ares I is based on a Shuttle solid rocket booster,

and carries the manned Orion spacecraft into low Earth orbit. Ares V is a heavy-lift launch vehicle that places the Altair Lunar lander into low Earth orbit. As currently designed, the Ares V is larger and capable of putting more payload into low Earth orbit than the Apollo Saturn V, which previously held the title of being the most powerful rocket ever launched.

1.1 Orion Crew Module

Figure 1.2: Orion spacecraft and support systems

Perhaps the most significant component of Constellation is Orion, the spacecraft that will take crew and equipment to the International Space Station, Moon, and beyond. The Orion spacecraft consists of the Service Module, which supplies fuel, oxygen, and main propulsion, and the Crew Module, in which astronauts will live and work during mission operations. Similar in concept to the Apollo Command Module, the Orion Crew Module is a truncated, conical blunt body designed for in-space operations and atmospheric entry. Also similar to Apollo and the Space Shuttle Orbiter, Orion will utilize computer-controlled atmospheric entry guidance and navigation.

1.2 Historical precedence

The research described herein is based, in part, on aeroballistic tests conducted at Aberdeen Proving Grounds in July of 2008, and associated investigations in (1). The research into these tests include a software suite that would take data from pressure sensors on the test article and iteratively solve for flight parameters such as angle of attack, sideslip angle, Mach number, and associated scale factors and biases on the pressure data, using a back-substitution method.

Figure 1.3: Pressure Transducer Model

At the time, only two ballistics tests had been conducted with fully instrumented test articles; these are referred to as Pressure Telemetry Modules 01 and 02. Previous test articles, used during similar aeroballistic tests conducted at Aberdeen in 2006, did not contain pressure sensors. PTM-01, in addition to the on-board inertial measurement unit (IMU), had five pressure sensors arranged in a cruciform shape. PTM-02 had an IMU and nine pressure sensors, identical to the format of later test articles.

1.3 Research goals

It is critical that the Orion on-board flight computer has accurate information concerning the aerodynamic properties of the vehicle. To this end, extensive wind-tunnel, CFD, and ballistics testing was conducted on scale models of Orion to establish a "library" of data on the aerodynamics and behavior of the vehicle. Once verified, the onboard flight computer will then have access to this library of data for use in compute flight trajectories and course corrections.

The analysis described in this document focuses on the recovery of various flight parameters from scale model aeroballistic testing. Two different recovery and reconstruction methods will be presented, including a pressure transducer-based method and an inertial measurement unit-based method.

Another significant aspect of this research was a statistical analysis of the existing methods utilized to compute pressure sensor-derived flight parameters. Systemic errors with previous analyses were examined, categorized, and reduced by improving the software, models, and methods.

Figure 1.4: Orion re-entry

1.4 Overview of investigation

This investigation is divided into four parts. Part I is an overview of the fundamentals of the problem, such as coordinate systems and flight parameter definitions, as well as a review of the aeroballistic testing that forms the basis of this investigation.

Part II is an analysis of the data from the inertial measurement unit, and discusses attempts at a trajectory reconstruction from that data.

Part III is an analysis of the pressure model, pressure data, and orientation reconstruction methods from that data. It concludes with a statistical analysis of the pressure solution.

Part IV is a summary of the resultant flight parameters, uncertainties, and pressure model coefficients, as well as a discussion of the various problems encountered with the reconstruction methods. It concludes with a discussion of future work and applications.

Part I: Fundamentals

2 Fundamentals

This section will review the topics and theories that form the basis of the investigation. A review of the aeroballistic testing will also be presented.

2.1 Coordinate systems

As with any engineering analysis, it is necessary to establish the relevant coordinate systems. A total of four different coordinate systems were used in the design and experimentation of the Orion scale model. They include:

- Inertial coordinate system (ICS)
- North-East-Down coordinate system (NED)
- Magnetic field coordinate system (MCS)
- Body coordinate system (BCS)

A thorough description and transformations between all four coordinate systems can be found in (1). Since the NED and magnetic field coordinate systems were not used in this analysis, only the inertial and body coordinate systems will be defined here.

2.1.1 Inertial frame

The inertial coordinate system is Earth-fixed with the origin at the exit of gun barrel. This is illustrated in Figure 2.1. Radar data was measured in a coordinate system that was rotated 180° about the *X*-axis. The radar coordinate system was rotated to align with the inertial coordinate system as defined above.

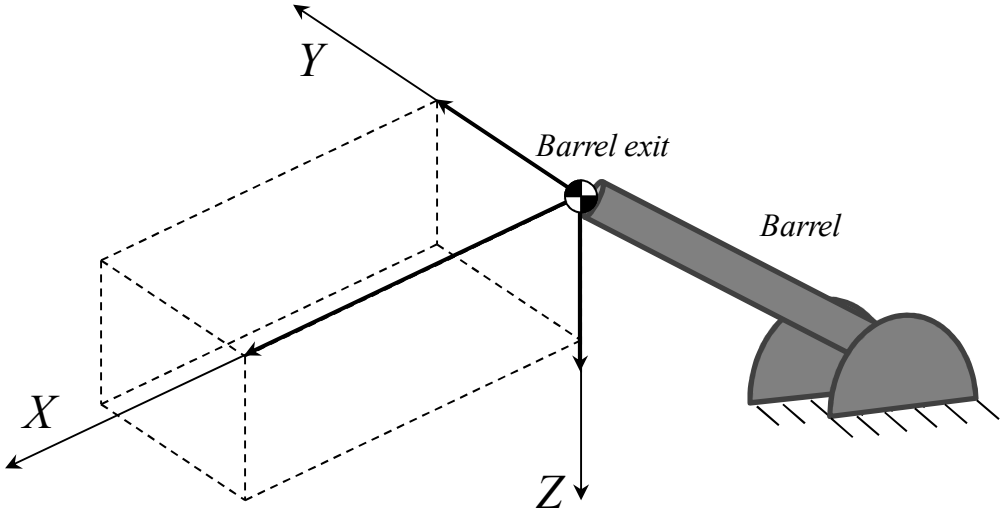

Figure 2.1: Navigation (inertial) coordinate system

2.1.2 Body frame

The body coordinate system is fixed to the vehicle with the origin at the center of mass and the *x*-axis pointing towards the center of the heat shield, along the axis of symmetry. This is illustrated in Figure 2.2.

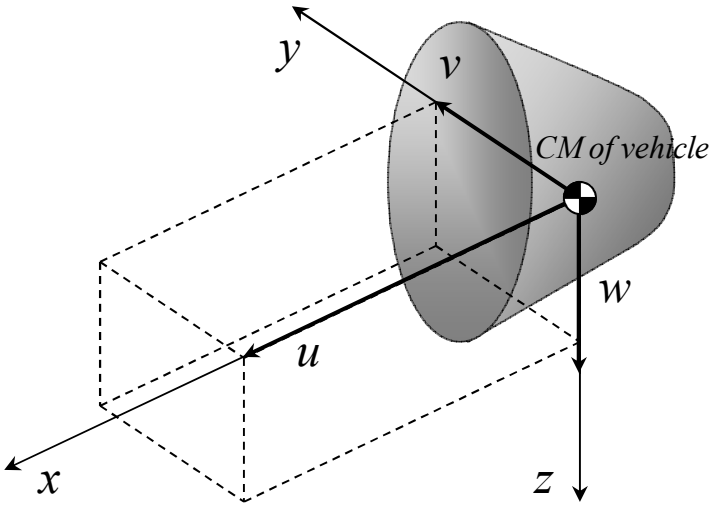

Figure 2.2: Body coordinate system

2.1.3 Transformations

By utilizing two vectors defined in two different frames, it is possible to compute a direction cosine matrix (DCM) that rotates one frame to the other. See Appendix A for the mathematical development of this method. The measured parameters in their respective coordinate systems are listed in Table 1.

Table 1: Measured parameters and coordinate systems

Body frame	
Parameter	**Source**
Velocity	Pressure (baseline)
Acceleration	Accelerometers
Magnetic field	Magnetometers
Inertial frame	
Parameter	**Source**
Velocity	Radar
Acceleration	Radar
Magnetic field	Constant

The second column of the table indicates how the velocity, acceleration, and magnetic field vector were observed or computed in both the body and inertia frames. The pressure-based velocity is derived from the pressure solution, which is discussed further in Part III.

Though not directly related to the coordinate systems discussed above, two angles are used to describe points on the surface of the heat shield. These are the clock and cone angles, and are illustrated in Figure 2.3. A scale drawing showing the cone angles is illustrated in Figure 3.6. The clock angle ϕ is measured from the upper vertical line of symmetry of the heat shield. The cone angle λ is measured from the axis of geometric symmetry.

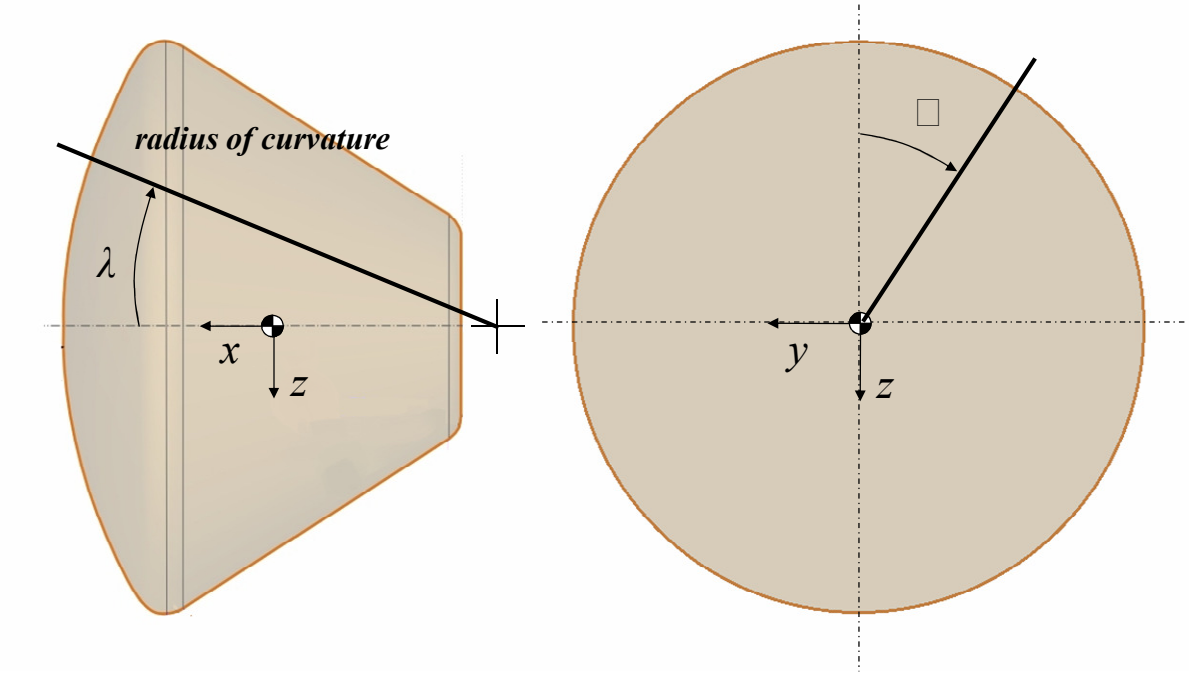

Figure 2.3: Clock and cone angle definitions (not to scale)

2.2 Flight parameters

The flight angles measure the difference between the body and wind axes, both of which have their origin at the vehicle center of mass. The wind *x*-axis is point along the velocity vector. The flight angles consist of angle of attack α, sideslip angle β, and total angle of attack α_T. These angles are illustrated in Figure 2.4.

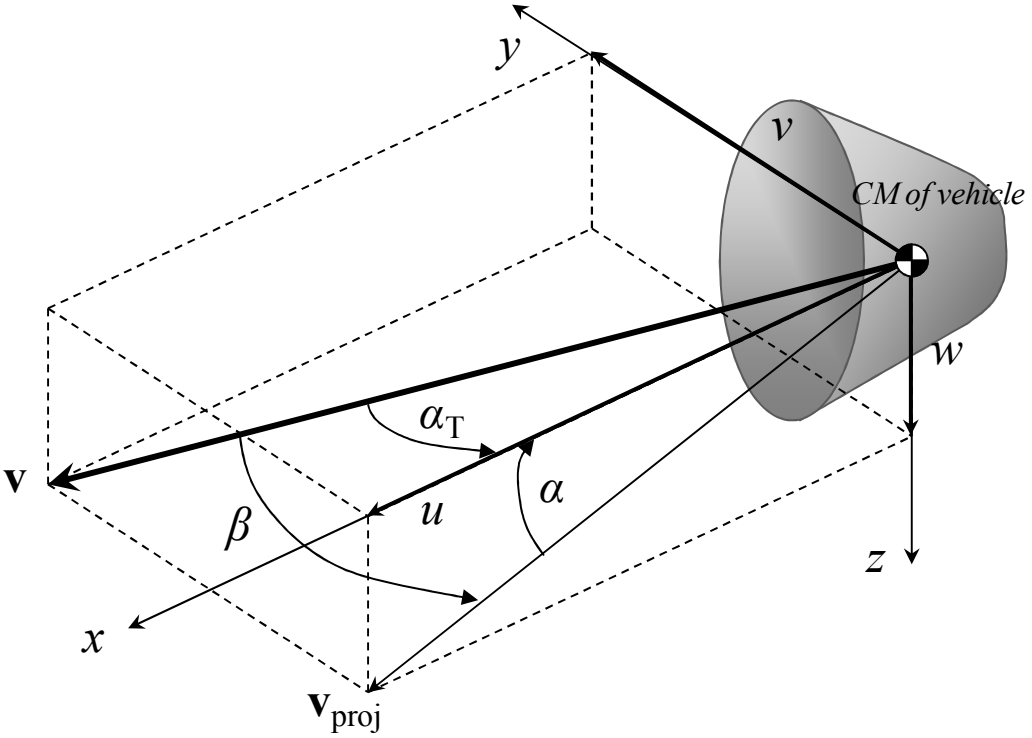

Figure 2.4: Direction of velocity vector in body coordinate system

The body frame velocities can be written in terms of the flight angles (2):

$$u = V \cos\alpha \cos\beta$$

$$v = V \sin\beta$$

$$w = V \sin\alpha \cos\beta$$

Likewise, the magnitude of the velocity vector and the flight parameters can be written in terms of these body velocity components (2):

$$V = |\mathbf{V}| = \sqrt{u^2 + v^2 + w^2}$$

$$\alpha = \tan^{-1}\frac{w}{u}$$

$$\beta = \sin^{-1}\frac{v}{V}$$

where $[u, V] > 0$. The total angle of attack can be written as

$$\alpha_T = \tan^{-1}\frac{\sqrt{v^2 + w^2}}{u} = \cos^{-1}(\cos\alpha \cos\beta)$$

The third and final flight parameter, Mach number, is derived from the total velocity:

$$M = \frac{V}{c}$$

where c is the velocity of the local speed of sound, which is computed using environmental parameters such as temperature and humidity. The computation of the speed of sound is derived in Appendix B.

Another important flight parameter is ψ, the clock angle of the wind vector:

$$\psi = \tan^{-1} \frac{\sin \beta}{\sin \alpha \cos \beta}$$

This angle is measured from the 0°, or upper vertical, clock angle (see Figure 3.7).

2.3 CFD database

A database containing CFD-based parameters was provided by previous CEV studies. The parameters included pressure and force coefficient values at various locations on the heat shield, total angles of attack, and Mach numbers. This database was used primarily to create the pressure models for the pressure data-derived trajectory.

3 Aeroballistics Testing

There have been five instrumented flights of the Orion test article, spread over three tests. These tests were conducted at Aberdeen Proving Grounds (APL), a US Army base in Aberdeen, Maryland. Test supervision and execution was provided by US Army Research Labs (ARL), a division of the Advanced Munitions Concepts Branch. The test history is summarized in Table 2. Each of the tests included a variety of non-instrumented calibration flights for the tracking cameras.

Figure 3.1: HARP gun at Aberdeen Proving Grounds

The gun used to fire the test articles was part of the Department of Defense's now-defunct High Altitude Research Program, or HARP. It is a 7-inch, smooth-bore gun designed to study the concept of placing small vehicles into orbit from a stationary firing unit. The program was also able to economically study the ballistics of these vehicles during re-entry. During the program's height in the 1960s, hundreds of small aeroballistic vehicles were

launched, with a HARP gun at Yuma, Arizona launching a payload to an altitude of 180 km (3).

Table 2: Summary of experiments at APL

Date	Test articles	Notes
April 2006	CEV-01 CEV-03 CEV-04 CEV-05	No pressure transducers
July 2008	PTM-01 PTM-02	01: 5 pressure taps 02: 9 pressure taps
July 2009	PTM-03 PTM-04 PTM-05	All three flights had 9 pressure taps; PTM-04 was a repeat of PTM-02

3.1 Pressure Telemetry Modules

The Pressure Telemetry Modules (PTMs) were the devices fired from the cannon in all five flights, an example of which is pictured in Figure 1.3. They consisted of titanium bodies machined into scale models of the Orion Crew Module. Each PTM contained sensors that transmitted data wirelessly to the control room.

Because the test site was a live-fire range, and the target area contained unexploded ordnance, the test articles could not be recovered after a flight. As a result, a PTM had to be manufactured for every test. PTM-02 through -05 were identical in outfit and design. PTM-01 had five pressure taps instead of nine, and will not be analyzed in this investigation.

The PTMs consisted of three segments, or plates. The titanium heat shield plate contained the nine 0.040”-diameter pressure taps. The middle stainless steel transducer plate contains the pressure transducers. The rear stainless steel plate contains the MIDAS sensor platform, which will be described in further detail in a later section of this document.

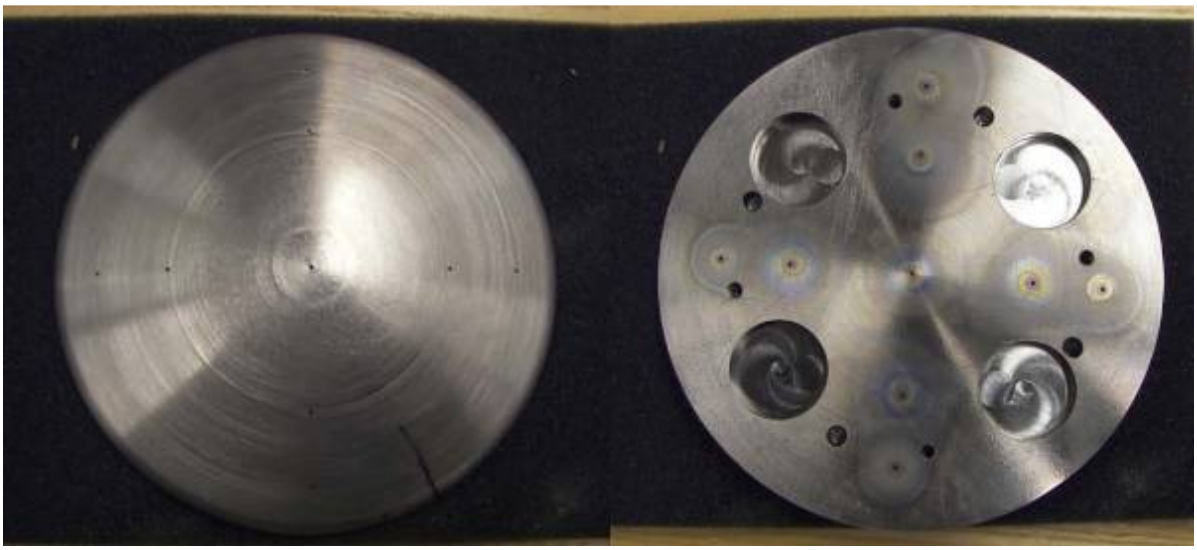

Figure 3.2: Heat shield plate

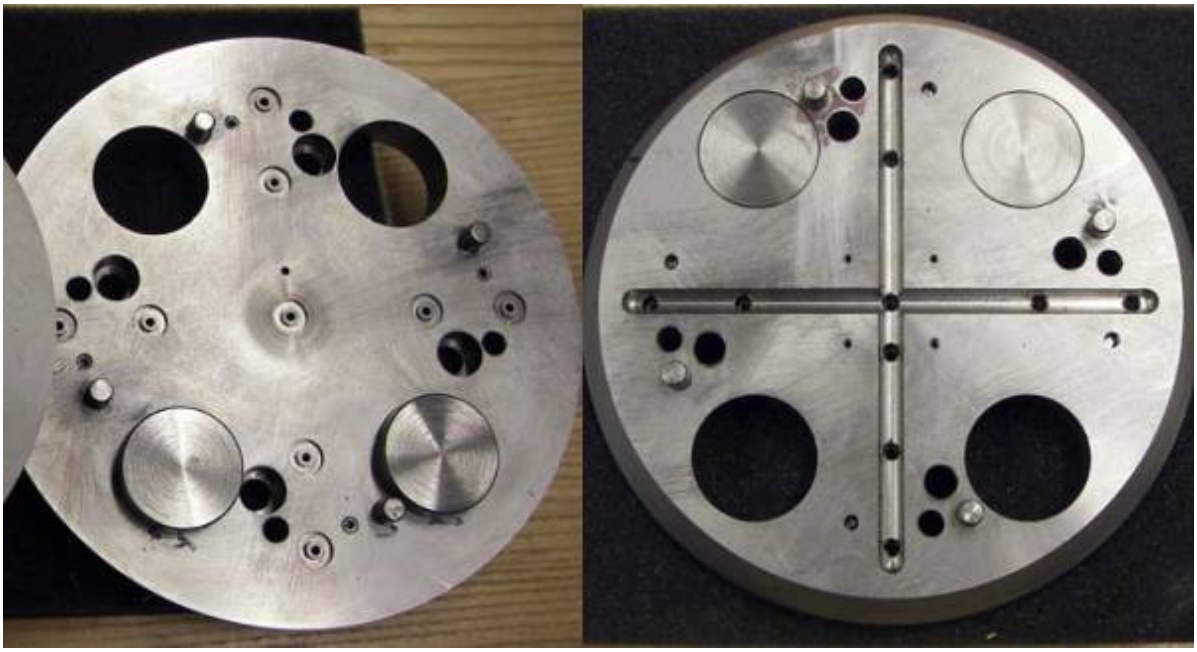

Figure 3.3: Transducer plate

Figure 3.4: Rear plate

Both the transducer and rear plates contain asymmetric weights that move the vehicle's center of gravity from the axis of symmetry, making it a lifting body.

3.2 Data sources

The data to be analyzed came from various sources, including an inertial measurement unit and pressure transducers located in the vehicle, as well as radar measurements taken on-site.

3.2.1 Onboard Instrumentation

The Orion test article contained a sensor suite that included commercially-available rate gyroscopes, 3-axis accelerometers, magnetometers, and pressure transducers. These are listed in Table 3.

Table 3: PTM Instrumentation

Sensor	Model #	Range	Measurement	Comments
Accelerometer	ADXSTC3-HG	+/- 8000 g	Acceleration along I	
Accelerometer	ADXL-278	+/- 250 g	Acceleration along I,J,K	Monolithic, dual-axis, high-g iMEMS
Accelerometer	ADXL-78	+/- 35 g	Acceleration along I,J,K	Monolithic, single-axis, high-g iMEMS
Rate gyro	ADXRS150	+/- 5500 dps	Angular rate about I,J,K	Single chip yaw rate gyro with signal conditioning
Rate gyro	ADXRS300	+/- 1200 dps	Angular rate about I,J,K	Single chip yaw rate gyro with signal conditioning
Magnetometer	HMC1043	+/- 3 Gauss	Magnetic field along I,J,K	3-axis surface mount array for low magnetic fields
Pressure transducer	XCEL-100	500 psi	Pressure normal to face of heat shield	Leadless sensor for static & dynamic environments

With the exception of the pressure transducers, all of the sensors were located on a cylindrical Multi-functional Instrumentation Data Acquisition System, or MIDAS, located inside the test article. Data were collected in real-time through an on-board, battery-powered wireless transmitter.

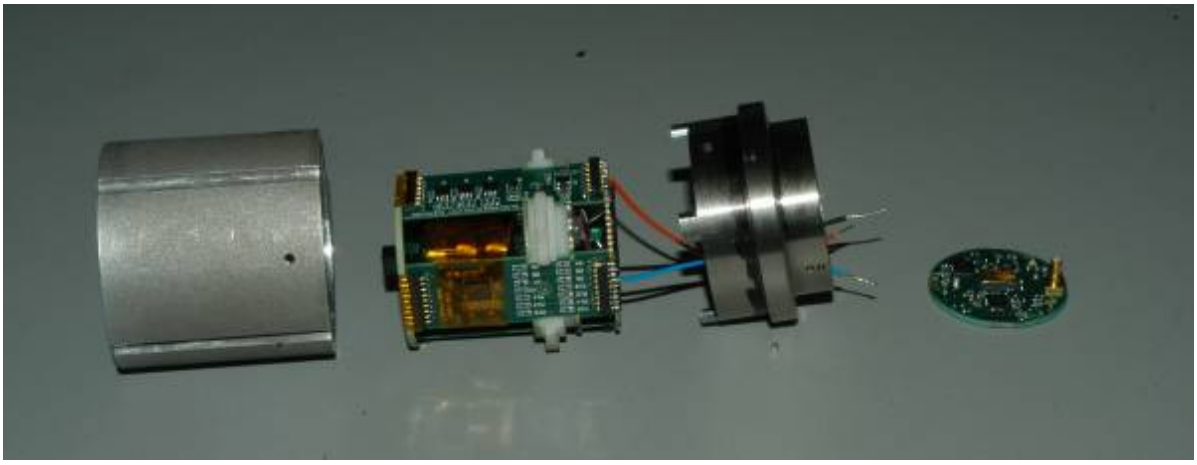

Figure 3.5: MIDAS stack

The pressure transducers were not inside this sensor platform, but located near the plane dividing the blunt heat shield region of the body from the upper conical region as illustrated in Figure 3.6. Each pressure transducer corresponds to a pressure tap, which are arranged in a cruciform shape on the heat shield. Four taps are located at the 19.45° and

12.59° cone angles each, and a single tap is located at the zero cone angle, or at the center of the heat shield. The arrangement of the pressure taps are illustrated in Figure 3.7.

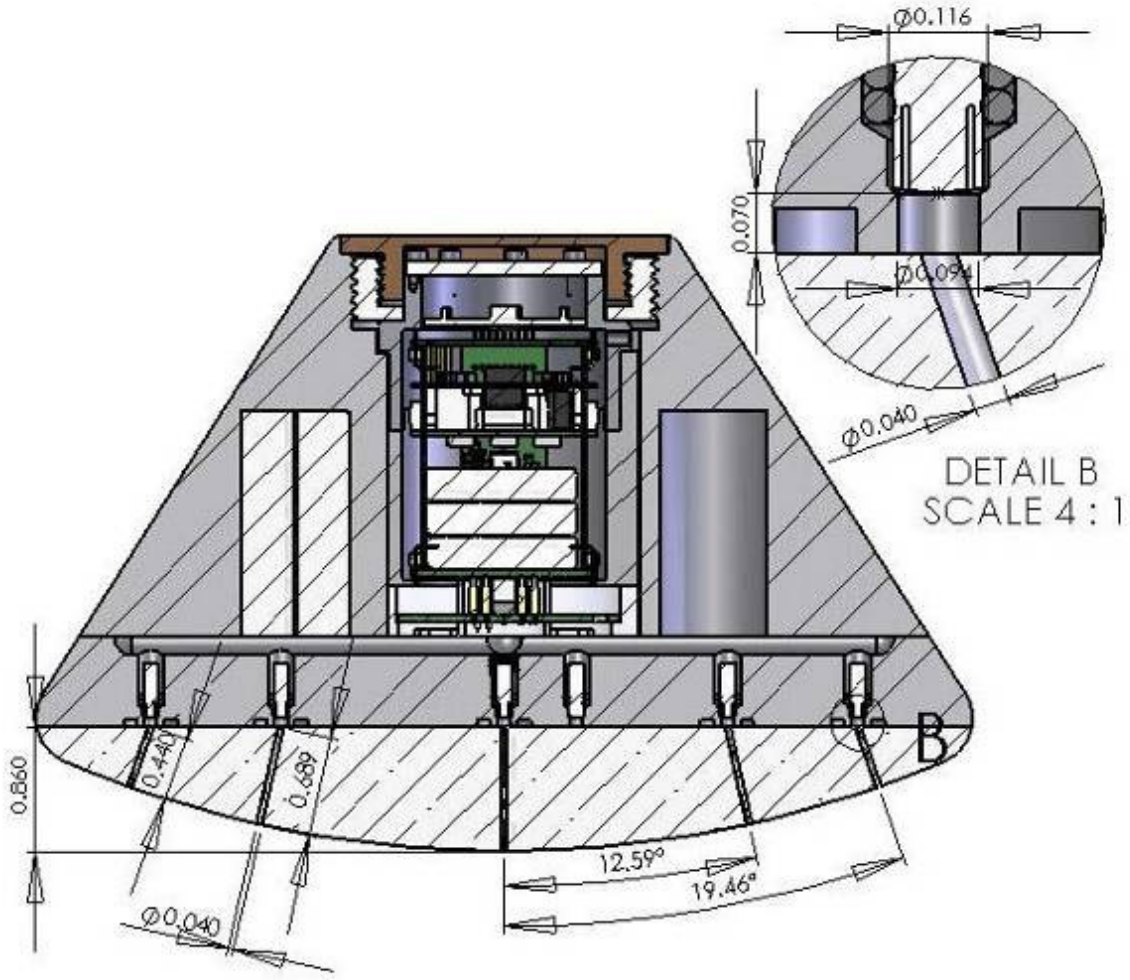

Figure 3.6: Cross-sectional view of PTM

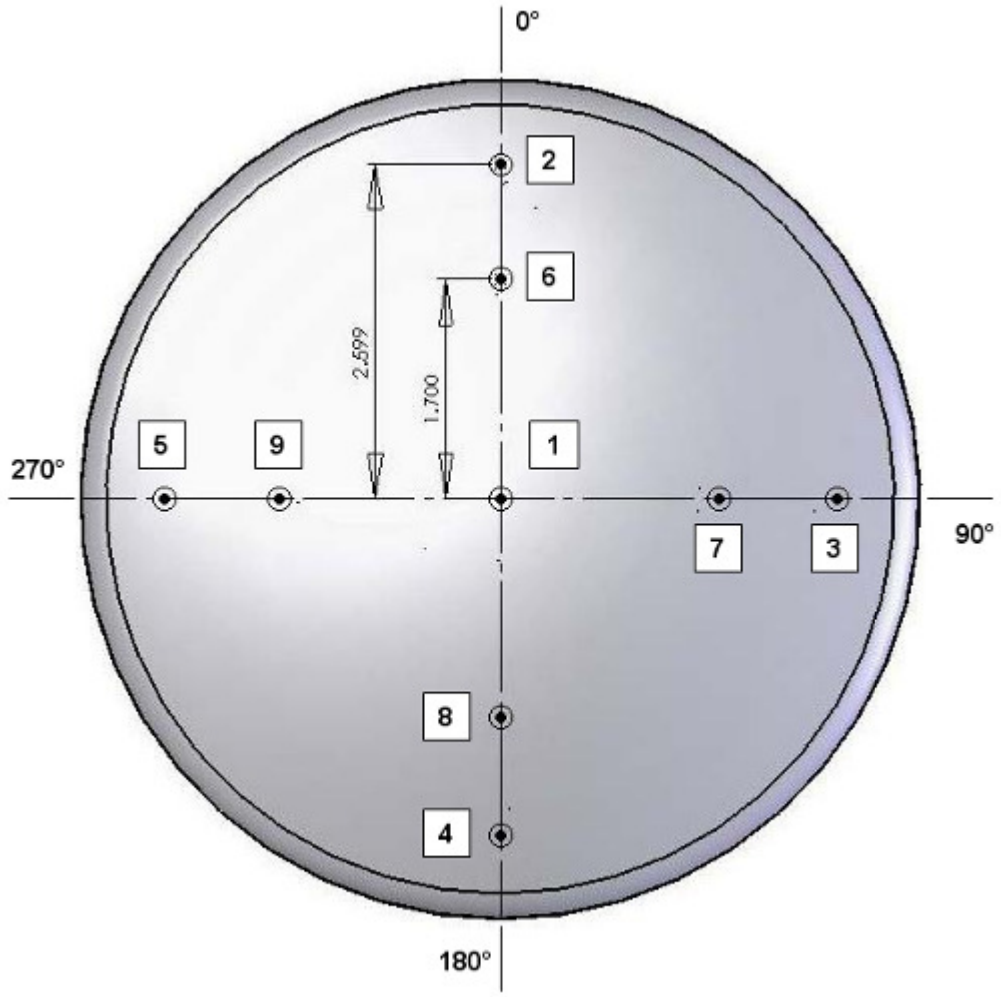

Figure 3.7: Pressure tap arrangement

3.2.2 Radar

The radar system was an azimuth and elevation monopulse tracker manufactured by Weibel Doppler Radars. A radar dish antenna was set up 49.8 meters behind and 11.7 meters to the left of the gun (see Figure 3.8). Collected radar data included vehicle position, velocity, acceleration, and Mach number as measured from the exit of the gun barrel.

3.3 Experiment setup and execution

3.3.1 Setup

As previously stated, the tests were conducted at Aberdeen Proving Grounds. The physical layout of the test site is illustrated in Figure 3.8.

For each test, identical pressure transducer models were constructed. Approximately two days prior to firing, the sensor suite was calibrated by Army Research Lab technicians to a pressure of approximately 90 kPa (1 p. 37). It is important to note that actual pressures observed during flight were as high as 1750 kPa (see Figure 7.1). The potential consequences of this calibration scheme are discussed further in Section 7.4.

Calibration shots were fired prior to actual tests, using blank, non-instrumented slugs to ensure that the high-speed cameras and radar tracked the vehicle properly.

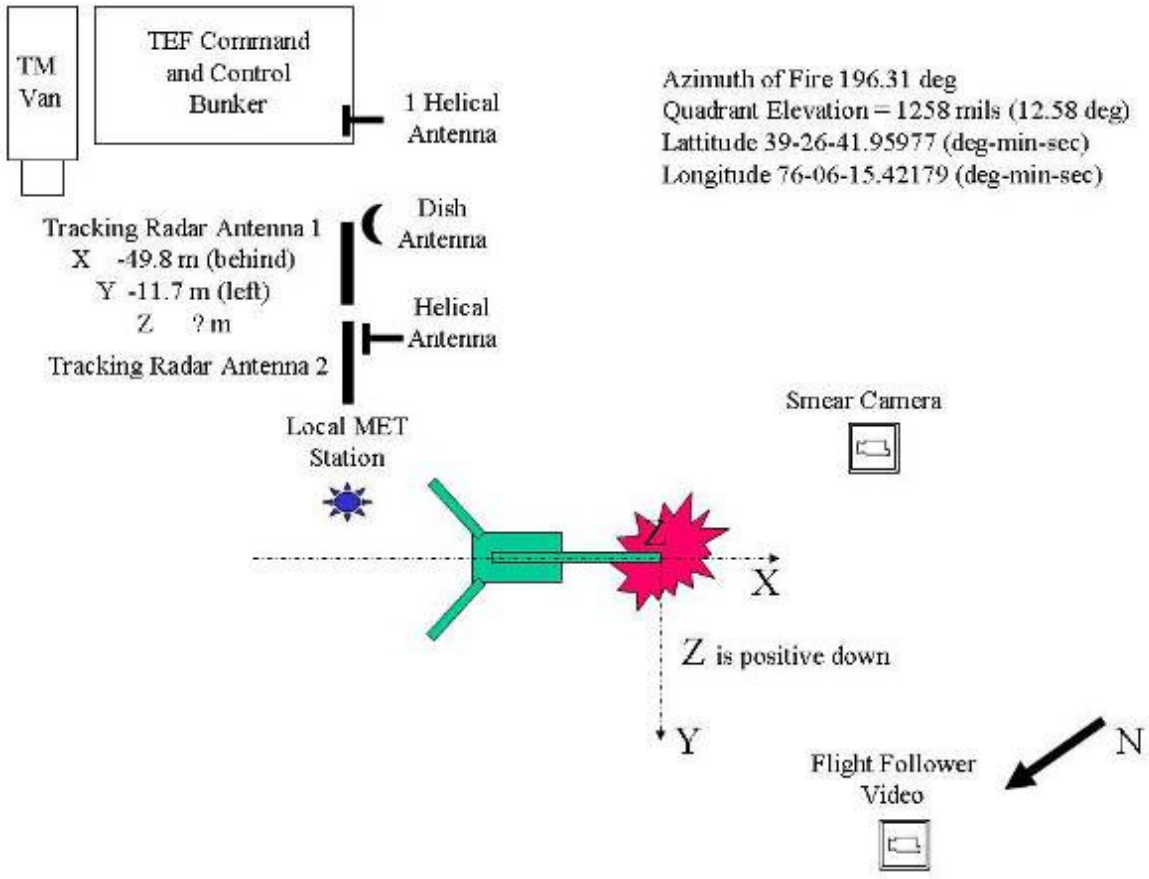

Figure 3.8: Layout of firing range (4)

Because the sensor suite was battery-powered, care was taken to activate the unit only when it was confirmed that the gun was ready. The PTM was then placed into a pre-fabricated sabot that orients the vehicle into a particular angle of attack and sideslip. The assembly placed into the firing chamber of the gun.

Figure 3.9: PTM inside sabot at non-zero angle of attack and sideslip

3.3.2 Execution

The first Orion test article fired during the second round of tests was PTM-04. This is because that particular Orion test article was found during calibration to have a faulty pressure port, number 8. Because the unit was already potted (that is, the sensor package was sealed into the model and removal would mean recalibrating all sensors, delaying the flights) it was decided that PTM-03 would be used on the flight that reproduced PTM-02. Reproducing the flight would supplement and verify the data from PTM-02.

PTM-05 was due to be mounted in the gun with a relatively high initial sideslip of 5°, as opposed to zero, to experiment with non-zero sideslip angles. When the non-instrumented calibration slug was fired at this orientation, however, the high-speed cameras captured the vehicle nearly tumbling into its secondary stable mode of conical-end first. In addition, the pressures measured were out of range of the database. For these reasons, data from PTM-02 were ignored.

Table 4: List of flights and relevant information

Flight	Date	α_0	β_0	Unused taps
PTM-02	7/14/2008	20	0	--
PTM-03	6/9/2009	20	0	4
PTM-04	6/8/2009	15	0	6, 8
PTM-05	6/9/2009	14.7	3.8	3, 5

3.4 Data recovery and processing

Because the sensor suite aboard the Orion test article was wireless, data was received by ground technicians in the telemetry van. Radar data and high-speed video were recorded by technicians in the command and control bunker, and video playback was instant. The data were converted from raw bits to engineering units on-site.

The official data from the second set of flights were delivered to the customer on 14 October 2009. The data were divided into various levels, each with a different degree of processing. These levels are:

- **Level 0:** Raw data. Level 0 data are signal bits taken directly from the sensors onboard the vehicle.
- **Level 1:** Delivered data. Level 1 data are data that have been converted to engineering units by Aberdeen Proving Labs.
- **Level 2:** Pre-processed data. Level 2 data is Level 1 data with a 7-point running mean applied and decimated to a time interval of 0.001 seconds.
- **Level 3:** Post-processed data. Level 3 data is Level 2 data with corrections applied to account for the center of mass location, signal mixing, and other errors.

The Level 3 data were used for further analysis.

Part II: Inertial Measurement Unit-based Solution

4 Radar and Inertial Measurement Unit Data Verification

The sensors aboard the vehicle measure a variety of parameters, from angular rates to accelerations to the strength of the local magnetic field. However, it is possible to compute some of these parameters through techniques that utilize different datasets, and compare them to the measured parameters. This section will describe the attempts to validate the IMU accelerometers and rate gyros using these methods, and their results. Radar-based verifications will also be discussed.

4.1 Accelerometer data

Body-frame accelerations are measured by the three-axis accelerometers in the inertial measurement unit. The acceleration histories measured by the accelerometers are shown in Figure 4.1.

Because the CFD database includes body force coefficients for a given set of total angle of attack α_T and Mach number M, it is possible to interpolate the force coefficients to the pressure-derived flight parameters. These axial and normal force coefficients are defined as

$$C_A = \frac{F_A}{q_\infty S}$$

$$C_N = \frac{F_N}{q_\infty S}$$

Recognizing that $F = ma$, the accelerations are then

$$a_A = \frac{C_A S q_\infty}{m}$$

$$a_N = \frac{C_N S q_\infty}{m} \cos\psi$$

$$a_Y = \frac{C_N S q_\infty}{m} \sin\psi$$

where S is the area of the heat shield on the vehicle, m is the mass of the vehicle, ψ is the clock angle of the wind vector (see Section 2.2), and q_∞ is dynamic pressure $q_\infty = \frac{1}{2}\gamma P_\infty M^2$.

The body accelerations a_A, a_N and a_y correspond to *x*-*y*-*z* components, respectively. These are the pressure and CFD-derived body accelerations, and are shown in Figure 4.1. Residuals are shown in Figure 4.2.

Examination of the figures reveals that the pressure-derived body accelerations are overestimating a_x by up to 200 m/s^2 in the supersonic regime. This could potentially be due to errors in interpolation caused by bad lookup values. Specifically, since the force coefficients being interpolated from the CFD tables are functions of M^2, any errors in the estimated Mach number would cause the interpolated values of the force coefficients to be incorrect, which would in turn give incorrect values of body-frame accelerations.

However, as will be established in Section 4.3 and seen in Figure 4.7, the pressure-derived Mach number agreed very well with the radar Mach number, with errors on the order of 5.0×10^{-3}. If the pressure-derived Mach number is indeed correct, then the error of 200 m/s^2 on the sensed accelerations could potentially have a catastrophic effect on the inertial reconstruction, as these accelerations will be integrated and errors would be compounded. This is, in fact, what was seen in the inertial reconstruction in Chapter 5. It is therefore more likely that the accelerometer data is inaccurate.

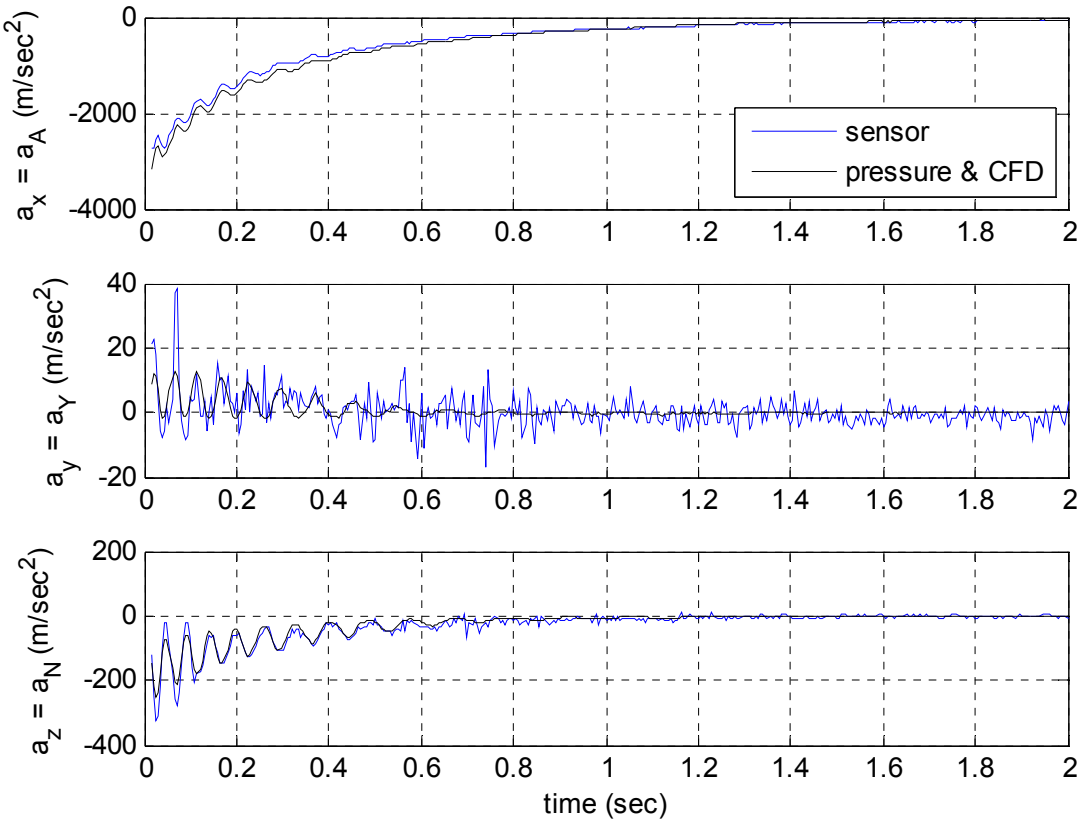

Figure 4.1: Body accelerations along axial, normal, and side directions

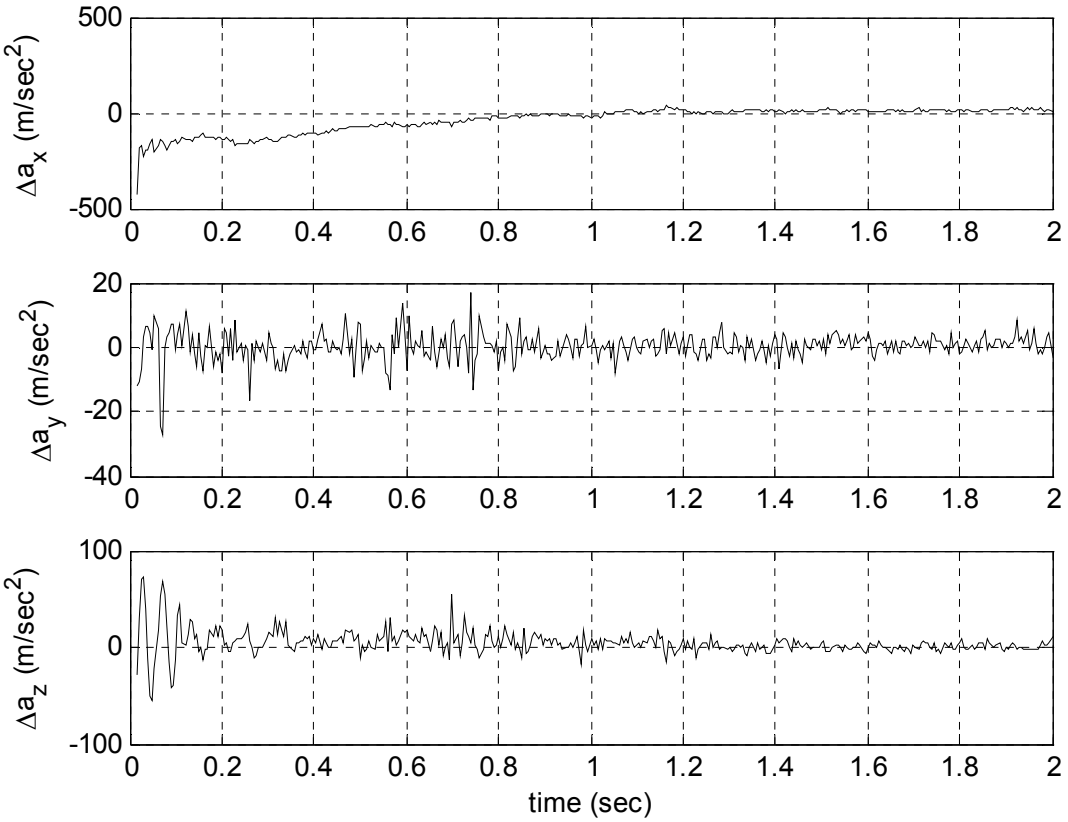

Figure 4.2: Residuals between sensor and pressure-derived body accelerations

4.2 Rate gyroscope and magnetometer data

Body-frame angular velocities are measured by the three-axis rate gyroscopes in the inertial measurement unit. The angular velocity histories measured by the rate gyroscopes are shown in Figure 4.5.

4.2.1 Magnetometer-derived body rates

Because the magnetometers measure the strength of the local magnetic field, and because the magnetic field vector is constant throughout the flight profile, it is possible to compute the angular velocities from the magnetometer data. Consider the equation for the time derivative of a vector in the inertial frame *a* (5 pp. 118-20):

$$\dot{\mathbf{v}}^b + \boldsymbol{\omega}^b \times \mathbf{v}^b = C_{ba}\dot{\mathbf{v}}^a$$

where C_{ba} is the DCM that transforms a vector from the inertial frame *a* to the body frame *b*. In this case, the vector of interest is the magnetic field strength **B**, which is constant in the inertial frame, that is, $C_{ba}\dot{\mathbf{v}}_a = 0$. Thus, the equation reduces to

$$\dot{\mathbf{B}} + \boldsymbol{\omega} \times \mathbf{B} = 0$$

where **B** and **ω** are the magnetic field and angular velocity vectors in the body frame, respectively. Rewriting this equation in matrix form and rearranging yields

$$\begin{bmatrix} 0 & B_3 & -B_2 \\ -B_3 & 0 & B_1 \\ B_2 & -B_1 & 0 \end{bmatrix} \begin{bmatrix} \omega_1 \\ \omega_2 \\ \omega_3 \end{bmatrix} = - \begin{bmatrix} \dot{B}_1 \\ \dot{B}_2 \\ \dot{B}_3 \end{bmatrix}$$

where $B_{1,2,3}$ and $\dot{B}_{1,2,3}$ are the *x*-*y*-*z* components of the magnetic field and its time derivative in the body frame, respectively, and $\omega_{1,2,3}$ are the *x*-*y*-*z* components of the angular velocity. Assuming that the roll rate ω_1 is known, the pitch and yaw rates can be computed solely from the magnetometer data by using linear least squares to solve the system of equations:

$$\begin{bmatrix} B_3 & -B_2 \\ 0 & B_1 \\ -B_1 & 0 \end{bmatrix} \begin{bmatrix} \omega_2 \\ \omega_3 \end{bmatrix} = - \begin{bmatrix} \dot{B}_1 \\ \dot{B}_2 - B_3\omega_1 \\ \dot{B}_3 + B_2\omega_1 \end{bmatrix}$$

These angular velocities are the magnetometer-derived rates. They are shown, along with the pressure-derived angular velocities discussed in the next section, in Figure 4.5. These plots assume the roll rate ω_1 is zero. Residuals are shown in Figure 4.6.

Examination of the figures reveals reasonably good agreement between rate sensor data and magnetometer-derived rates. The relatively high residuals in the pitch rate can be attributed to a slight phase lag between the sensor and magnetometer-derived rates.

4.2.2 Pressure and CFD-derived body rates

Body-frame angular velocities can also be approximated using angle of attack and sideslip histories, for example, $r \cong \dot{\beta}$. However, it is necessary to take into account the flight path angle γ. The relationship between the flight path angle γ, angle of attack α, and pitch angle θ in the inertial frame is illustrated in Figure 4.3.

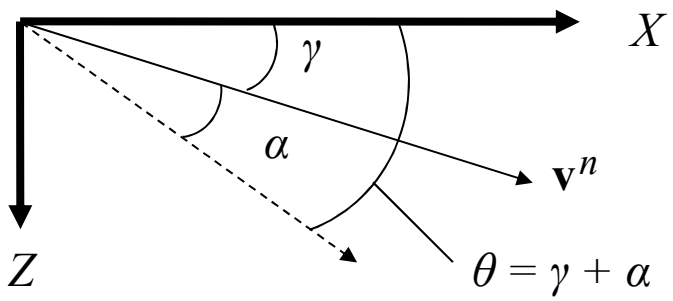

Figure 4.3: Relationship between flight path angle γ, angle of attack α, and pitch angle θ

The flight path angle is the angle between the inertial velocity vector $\boldsymbol{v}^n = [u \ v \ w]$ and the local horizontal $\boldsymbol{x}^n = [0 \ 0 \ 1]$, where *n* denotes the inertial frame. From the definition of the dot product,

$$\sin\gamma = \frac{\boldsymbol{v}^n \cdot \boldsymbol{x}^n}{|\boldsymbol{v}^n||\boldsymbol{x}^n|} = \frac{w}{|\boldsymbol{v}^n|}$$

Taking the time-derivative of $\sin\gamma$ yields

$$\cos\gamma\,\dot{\gamma} = \frac{\dot{w}}{|\boldsymbol{v}^n|} - \frac{w(u\dot{u} + v\dot{v} + w\dot{w})}{(u^2 + v^2 + w^2)^{3/2}}$$

which in turn gives the time-derivative of the flight path angle:

$$\dot{\gamma} = \frac{\dot{w}}{|\boldsymbol{v}^n|\cos\gamma} - \frac{w(u\dot{u} + v\dot{v} + w\dot{w})}{\cos\gamma\,(u^2 + v^2 + w^2)^{3/2}}$$

The flight path angle and flight path angle rate are shown in Figure 4.4. The "spikes" seen in the flight path angle rate are due to a flattening in the flight angle curve. The $\dot{w}$ term, which corresponds to inertial *Z* acceleration (refer to Figure 4.4), also exhibits sharp spikes. These phenomena are caused by effects of the radar dish's side lobes.

Pitch rate can now be computed:

$$\omega_2 = \dot{\theta} = \dot{\gamma} + \dot{\alpha}$$

This is the pressure-derived pitch rate, which is shown in Figure 4.5.

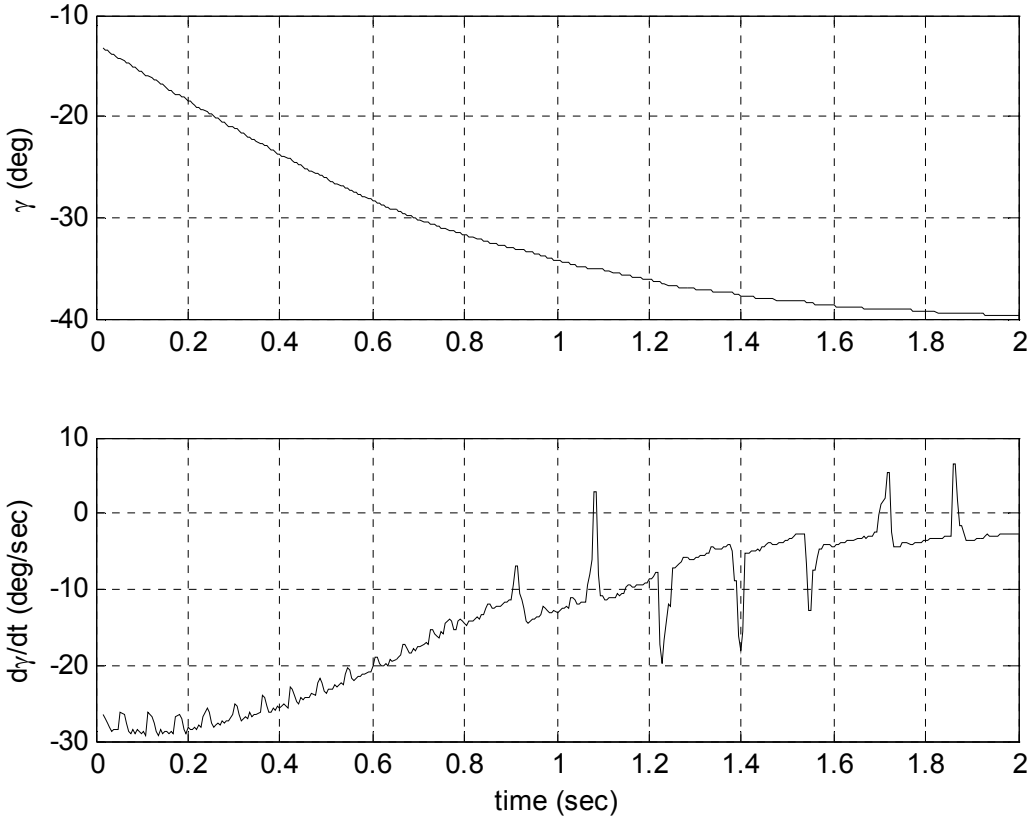

Figure 4.4: Flight path angle and flight path angle rate

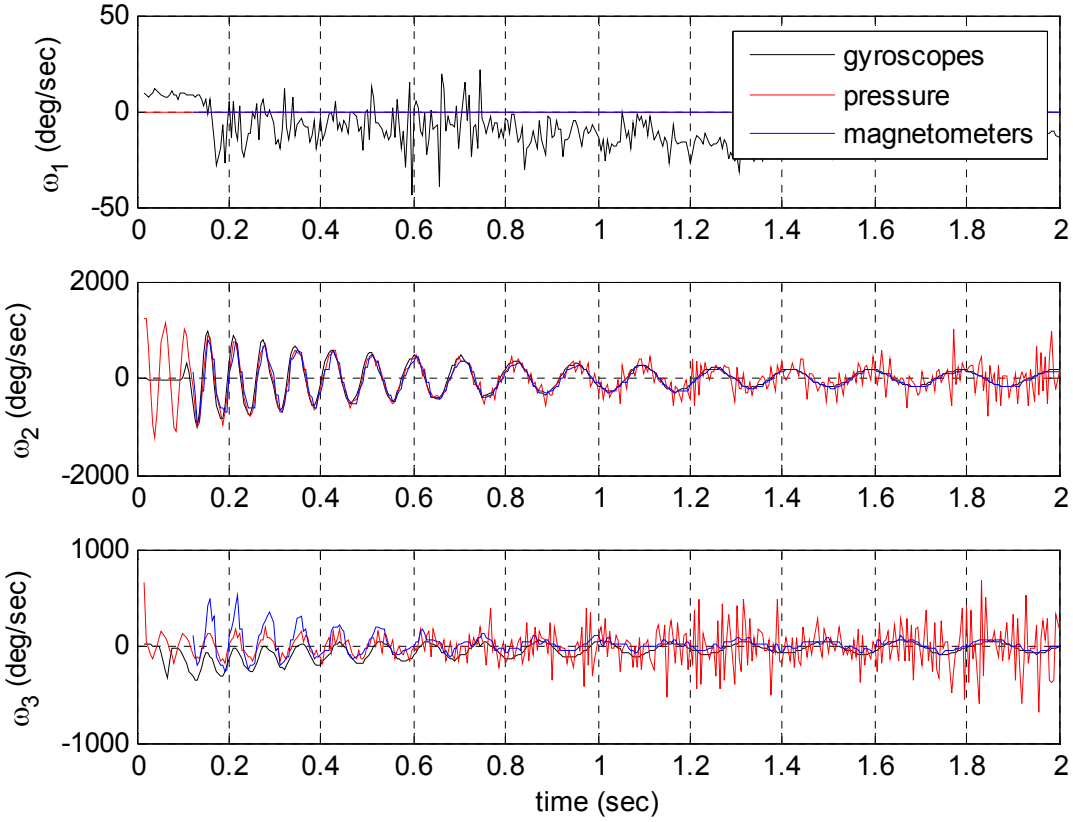

Figure 4.5: Angular velocities

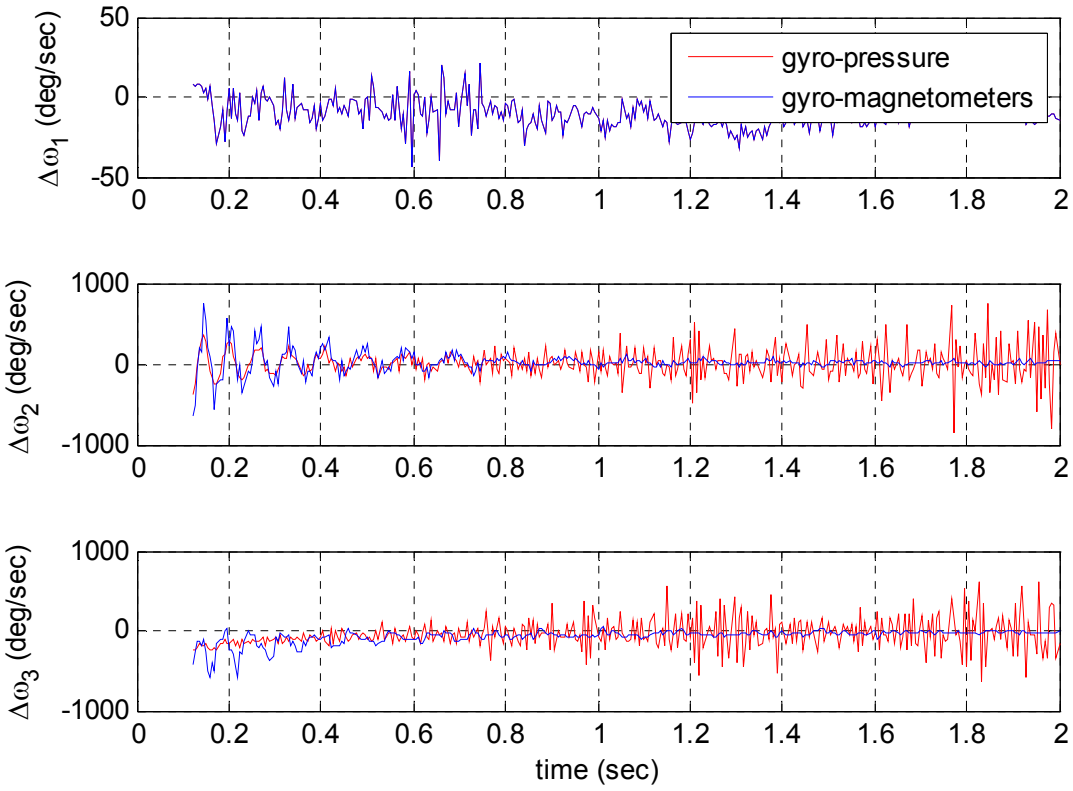

Figure 4.6: Residuals between rate gyro, pressure, and magnetometer-derived angular velocities

4.3 Radar data

By its nature, all radar data is measured in the inertial frame. Along with the magnetic field vector, the measured parameters in the inertial frame include vehicle position, velocity, and acceleration (See Table 1). To verify the radar data, it is useful to compare radar-derived flight parameters with those derived from pressure.

4.3.1 Mach number

Because part of the radar data was Mach number, a direct comparison between the radar-measured Mach number and pressure-derived Mach number can be made. This is shown in Figure 4.7.

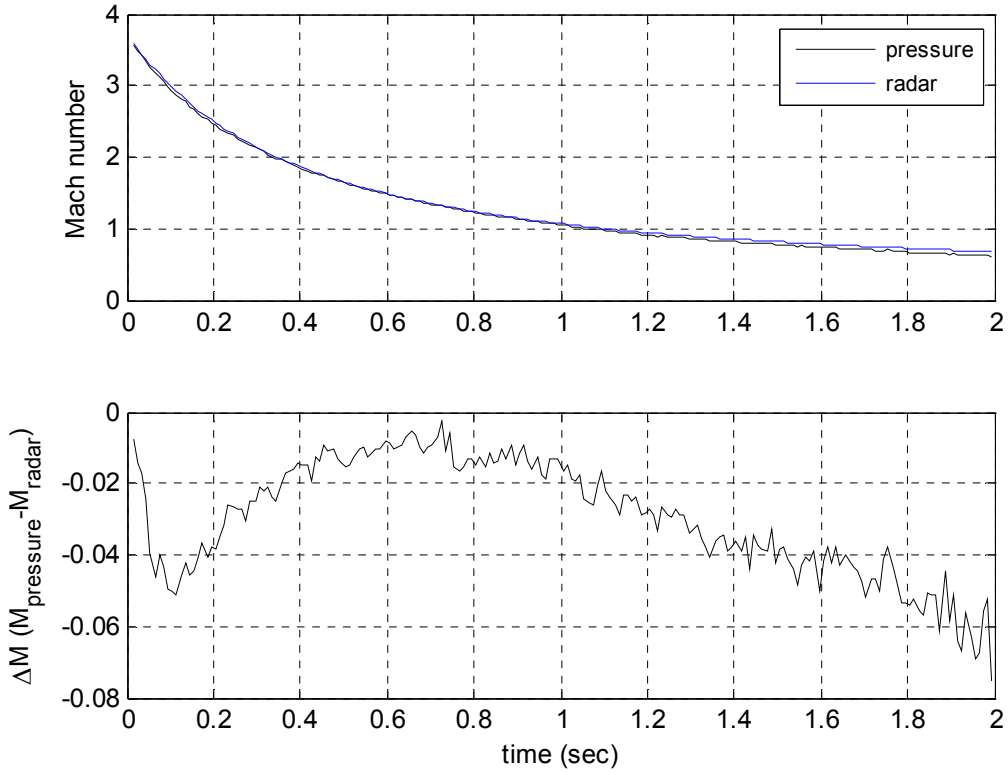

Figure 4.7: Comparison of pressure-derived and radar Mach number, PTM-02

Examining the figure reveals that the radar is overestimating the Mach number by 0.05 immediately after the vehicle is launched and after it reaches subsonic velocities (at approximately 1.10 seconds).

4.3.2 Flight angles

The flight angles are computed from the body velocities as described in Section 2.2. Since body velocities are not directly observable in these experiments, it is necessary to transform the inertial velocities to the body frame. To do this, two vectors described in two frames are needed to create a DCM, which can be computed using the triad method. The mathematical derivation of this method is described in Appendix A.

Once the DCM that rotates from the inertial frame to the body frame is computed for every measurement in time, the DCM history can be applied to the radar velocity to get the body frame velocity:

$$\mathbf{v}^b = C_{bn}\mathbf{v}^n$$

From these radar-derived body velocities, the flight angles can be computed. These are shown in Figure 4.8. Residuals are shown in Figure 4.9.

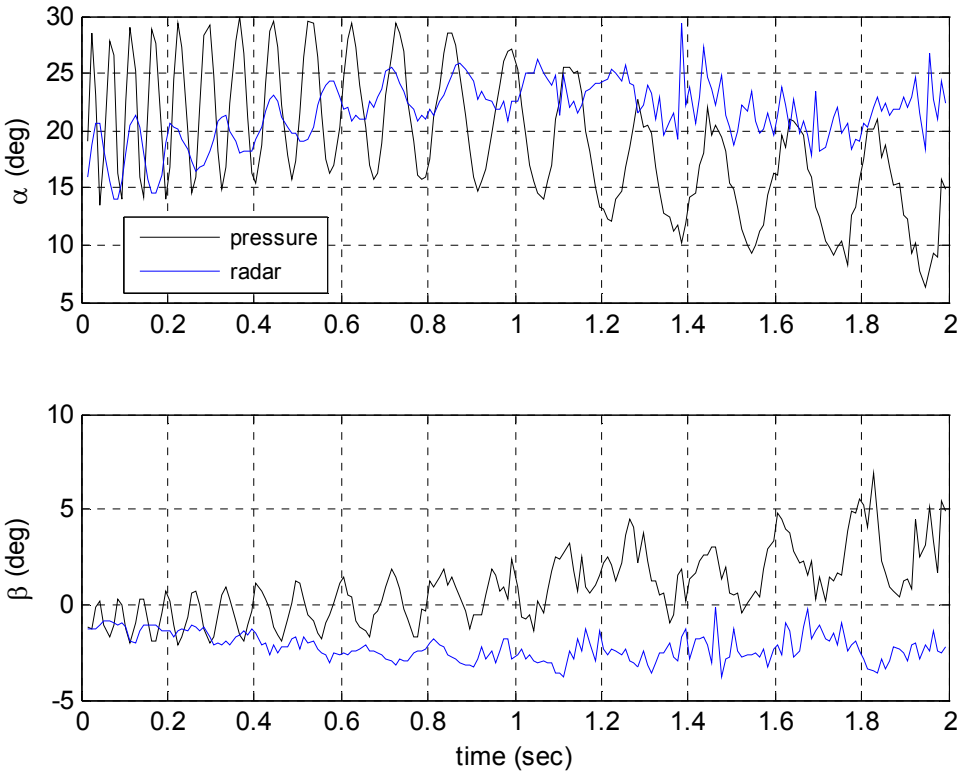

Figure 4.8: Comparison of pressure-derived and radar-derived flight angles

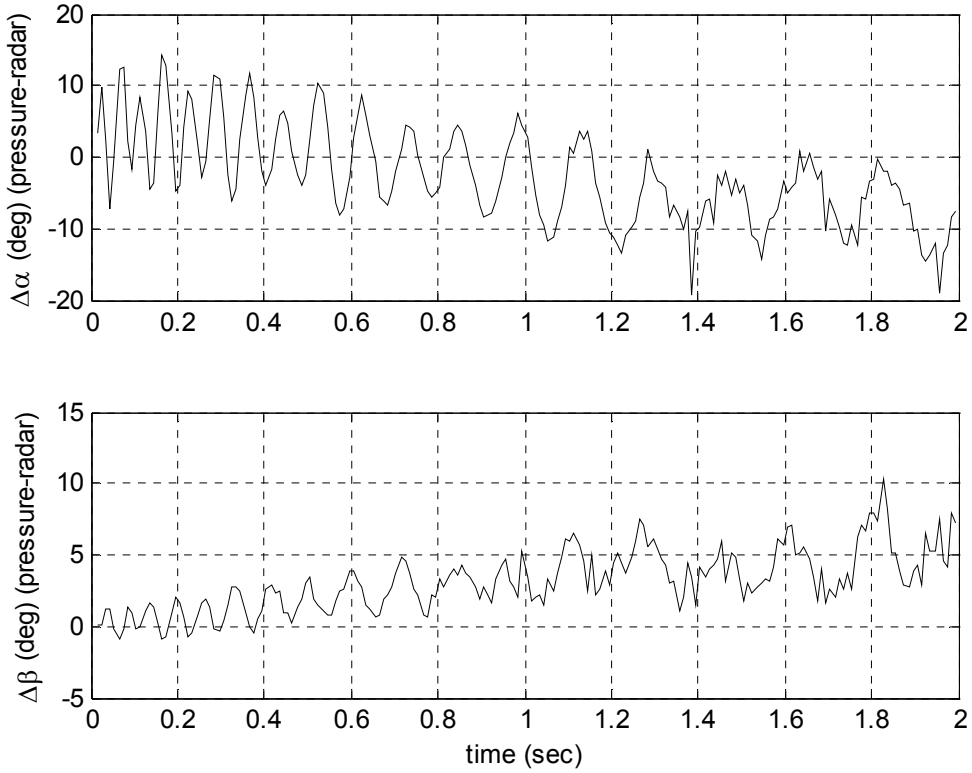

Figure 4.9: Residuals between pressure and radar flight angles

Examining the figure reveals that the radar-derived flight angles generally follow the long-term pressure-derived α and β trends. However, the amplitude of the radar oscillations do not match those of pressure flight angles. This is due to the fact that the radar data has been smoothed in post-processing prior to delivery, which effectively eliminates any high-frequency oscillations that may have been captured by radar. For this reason, it is unlikely that radar data can be used to validate flight parameters that have high-frequency body oscillations, such as angle of attack and sideslip angle.

4.4 Discussion of IMU data

In this Chapter, we have discussed several different ways to independently verify the data from the sensors aboard the IMU. While at first the sensors appear to be reasonably

validated, unfortunately using them for a reconstruction does not yield acceptable results, due to the high sensitivity of the IMU-based reconstruction on the angular rates.

5 Recovery of Flight Parameters from Inertial Measurement Unit Data

As part of the research conducted into the Orion test article aeroballistics tests, the trajectory of the vehicle was computed using only the sensors aboard the Multi-functional Instrumentation Data Acquisition System, or MIDAS. The use of MIDAS data serves as a "double-check" of the pressure-derived flight parameters. Unfortunately, as will be explained later in this section, the data recorded by the MIDAS sensors were not of the necessary quality to accurately reconstruct the trajectory. Nevertheless, the process for trajectory recovery using quaternions will be discussed.

5.1 Initial conditions

To begin the reconstruction, the orientation of the Orion test article at the initial time frame must known. Because the reconstruction must start when sensors begin transmitting useful data, and because that time point occurs after the test article has cleared the gun barrel, this initial orientation is not that of inside the barrel. Figure 5.1 illustrates how the rate gyros did not start transmitting useful data together until roughly 0.15 seconds after zero-time (muzzle exit). The distortions from -0.03s to 0.02s were generated by the chamber explosion and were not considered "real" data.

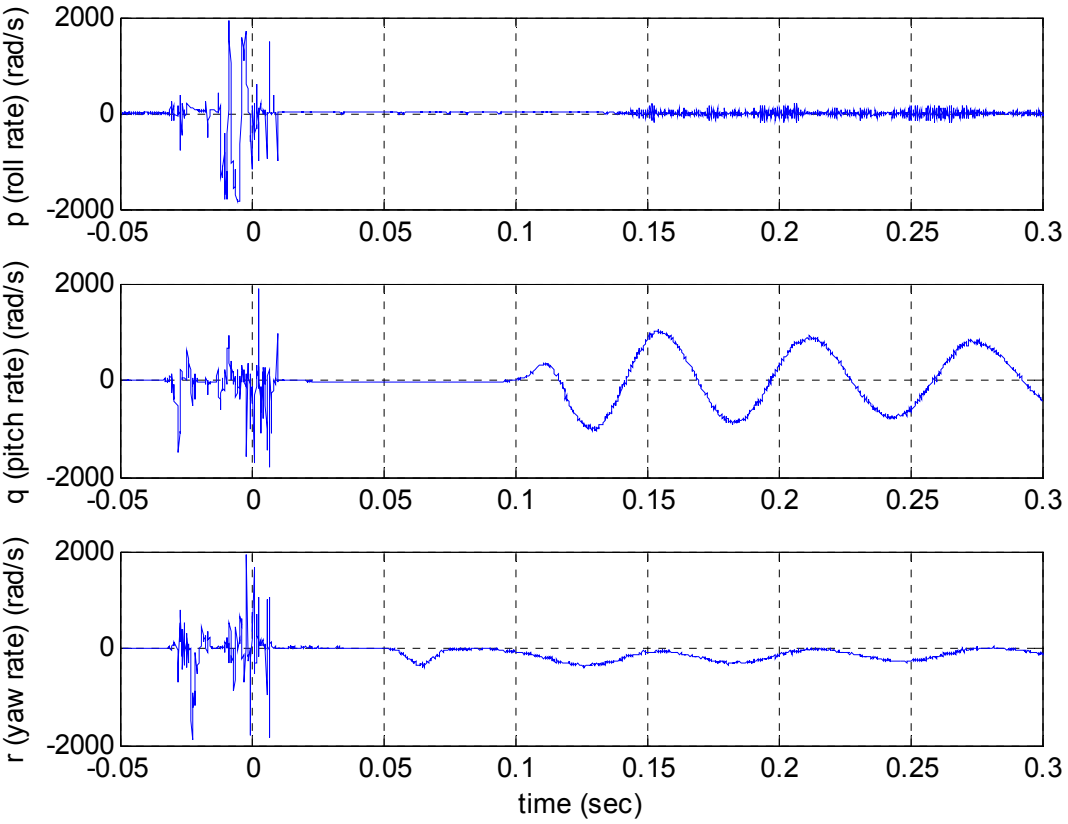

Figure 5.1: Observed initial body rates

The initial orientation was computed by finding a direction cosine matrix that transformed vectors between the navigation and body frames (using magnetometer and velocity data), and extracting the Euler angles from that DCM. Before this DCM was computed, however, the magnetometer data was "corrected" to force its normalized magnitude to be a constant 0.524 Gauss throughout the flight.

5.1.1 Correction of magnetometer data

The magnetometer data were corrected by using a linear least-squares approach, which solved for biases, scale factors, and misalignments:

$$\widetilde{\boldsymbol{B}}^b = \begin{bmatrix} \tilde{B}_x^b \\ \tilde{B}_y^b \\ \tilde{B}_z^b \end{bmatrix} = \begin{bmatrix} Bias_x + SF_x B_x^b + \Delta\theta_y B_z^b - \Delta\theta_z B_y^b \\ Bias_y + SF_y B_y^b - \Delta\theta_x B_z^b + \Delta\theta_z B_x^b \\ Bias_z + SF_z B_z^b + \Delta\theta_x B_y^b - \Delta\theta_y B_x^b \end{bmatrix}$$

where $\widetilde{\boldsymbol{B}}^{b}$ is the corrected magnetic field vector in the body frame.

5.1.2 Euler angles from DCMs

A direction cosine matrix that transformed orientations between the body and inertial frames was computed for each time point. This DCM history was computed using the triad method described in Appendix A, with the following vectors as the bases (listed with their source):

- Velocity in the inertial frame (radar)
- Magnetic field vector in inertial frame (constant)
- Velocity vector in body frame (pressure solution)
- Magnetic field vector in body frame (magnetometers, corrected)

From the elements of this DCM, which is a 3-2-1 Euler angle rotation, the Euler angles can be computed:

$$\tan\phi = \frac{C_{bn}(2,3)}{C_{bn}(3,3)}$$

$$\sin\theta = C_{bn}(1,3)$$

$$\tan\psi = \frac{C_{bn}(1,2)}{C_{bn}(1,1)}$$

where C_{bn} is the DCM that transforms a vector from the inertial frame *n* to the body frame *b*. The initial orientation is the first set of Euler angles in the Euler angle history.

5.2 Data adjustments

5.2.1 Adjustment of body angular rates

Studying the rate gyro data from Figure 4.5, it can be seen that the yaw rate does not oscillate about zero. In addition, the rate gyros have a linear acceleration effect of 0.20 deg/sec/g (6). Because total acceleration in the supersonic regime can exceed more than 250 g's (see Figure 4.1), it was postulated that it would be advantageous to apply a scale factor and bias to the to the rate gyros, in order to provide a better flight angle solution.

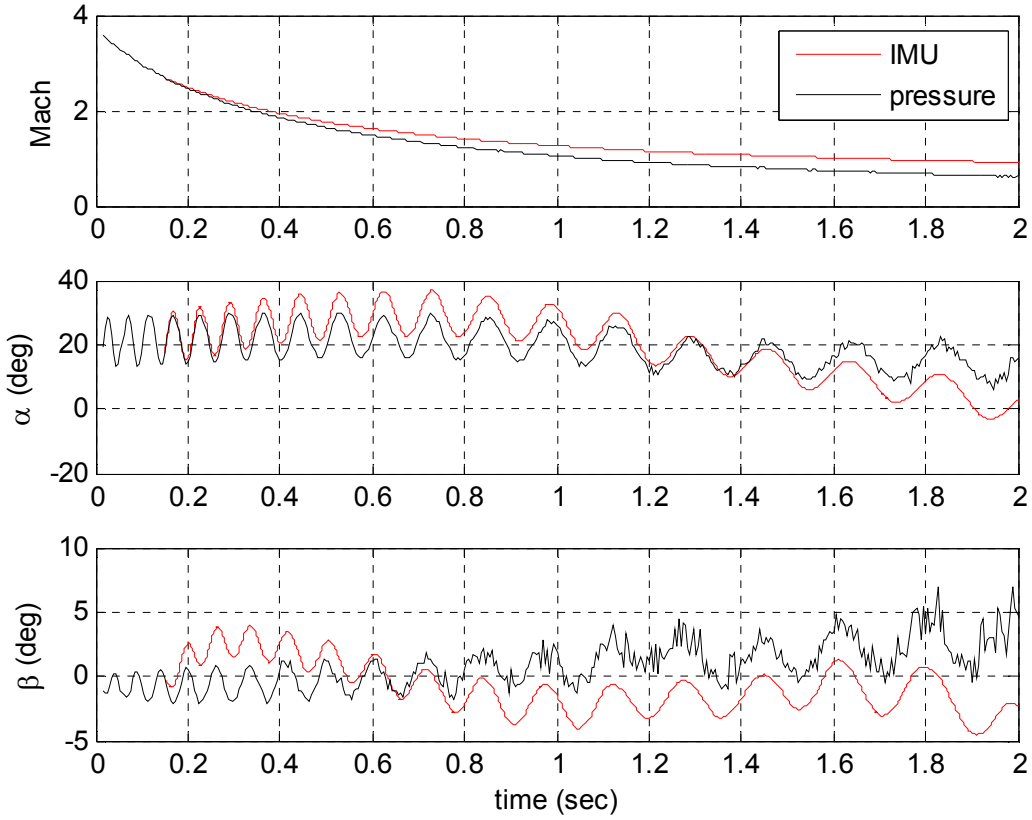

Figure 5.2: IMU reconstruction, adjusted yaw rate

Figure 5.2 shows the IMU reconstruction solution after the yaw rate has been forced to oscillate about zero by subtracted a quadratic best-fit from the rate. In addition, a constant bias of -0.50 rad/sec has been added to the yaw rate. Clearly, the solution has improved in both angle of attack and sideslip angle when compared to Figure 5.4, but as the next section will demonstrate, the solution can be improved even further.

5.2.2 Magnetometer-derived body rates in IMU reconstruction

From Figure 4.5, it can be seen that the rate sensor data has some problems, as the amplitude and trend in the supersonic regime do not correspond to those in the magnetometer- and pressure-derived rates. Improvements to the IMU-based reconstruction can be made by instead using the magnetometer-derived rates. Pressure-derived rates were not used, as it was the pressure-derived flight parameters that were being verified.

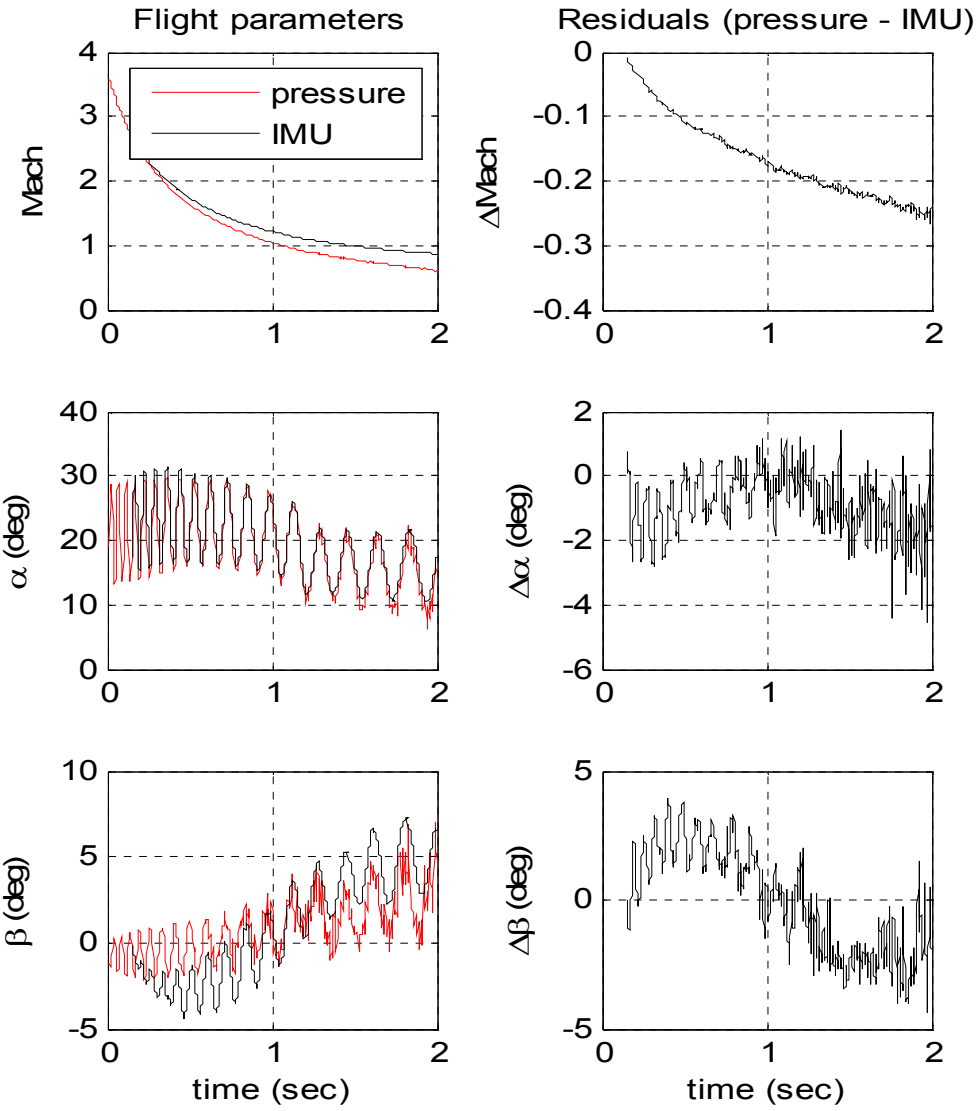

Figure 5.3: IMU-based flight parameters, adjusted magnetometer-derived angular rates

Clearly there is an improvement when switching to adjusted magnetometer-derived rates, but problems with Mach number and sideslip angle persist. Currently, this is the best-case IMU-based solution available.

5.3 IMU-derived trajectory and flight parameters

Figure 5.4 shows the IMU-based flight parameters if no adjustments are made to any of the sensors. Clearly these angles are incorrect, since the vehicle did not immediately rotate 50 degrees upon launch (verified by flight video). In addition, the Mach number increases after one second, which is of course impossible. When compared to the flight parameters in Figure 5.3 found by using adjusted sensors and substituting in the magnetometer rates for the sensed rates, this trajectory is unacceptable.

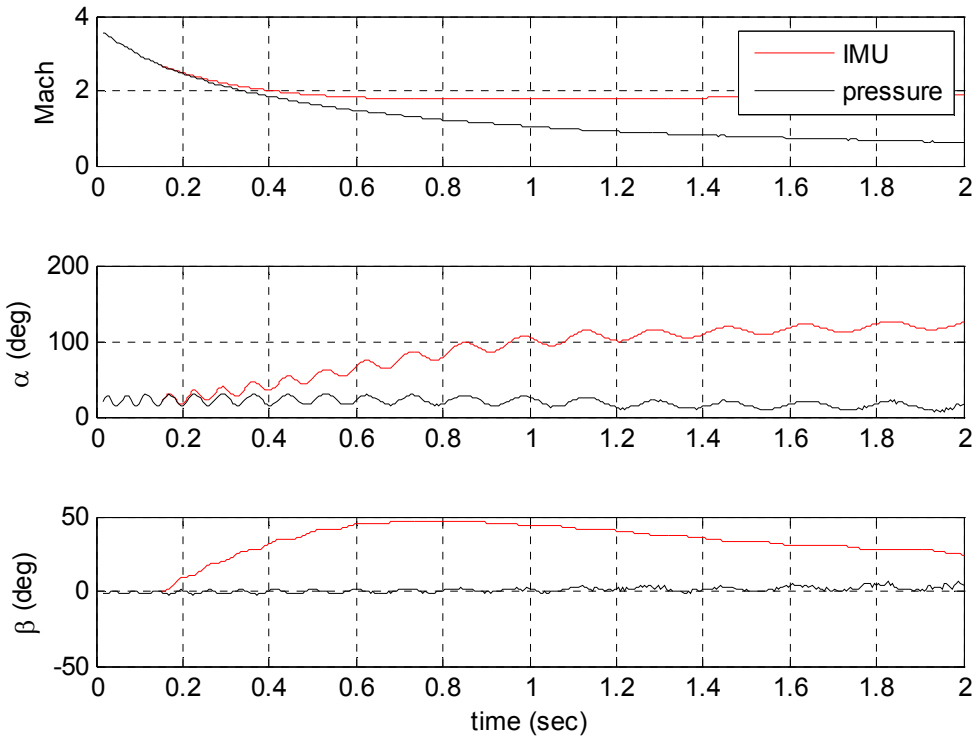

Figure 5.4: IMU-based flight parameters, no adjustments

5.4 Discussion of problems with IMU reconstruction

The trajectory reconstruction was carried out as described in Appendix C. In this case, the magnetometer-derived angular rates were used instead of rate gyro data, due to the bias and scale factor problem present in the z-axis rate gyro. Unfortunately, the trajectory

(position, velocity, and acceleration) deviated immediately and significantly from the radar trajectory, and is not reproduced in this thesis. Several possibilities exist for this.

As alluded to in Chapter 4 and previous Sections in this Chapter, there are several problems that can be identified with the IMU data.

1. Rate gyros: The rate gyros are perhaps the most critical component of the IMU reconstruction. For the rate gyros, the orientation of the body can be determined through integration. As such, small errors in the sensed rates can lead to large errors in orientation, even when the sensed rates appear to agree with the derived rates from independent sources (Figure 4.5). Attempts to correct these rates for use in the IMU reconstruction are discussed in Section 5.2.1.
2. Accelerometers: The accelerometers also play an important role in the IMU reconstruction. The bias in a_x shown in Figure 4.1, when compared to the pressure and CFD-derived x-acceleration, would have a strong effect on the trajectory and orientation when its magnitude is considered.
3. Magnetometers: The magnetometers measure the strength of the local magnetic field vector in the body frame, and the magnitude of the magnetic field vector is expected to be constant over the relatively short distance the vehicle travels. However, the magnetometers measured a variable magnitude, which ranged from 0.42 to 0.64. Attempts to correct this are discussed in Section 5.1.1.

These problems prevented the computation of a reliable IMU-based orientation history. While its results can be retained as a qualitative verification of the flight parameters, Part III of this thesis will show that the pressure-based solution is considerably more dependable.

Part III: Pressure-based Solution

6 Pressure Model Analysis

A method of recovering vehicle orientation utilizes the nine pressure sensors and taps located on the blunt end of the test articles (note that because each pressure sensor corresponds to a single pressure tap, both terms will be used interchangeably). The pressure data was fed into a MATLAB software package, which returned reconstructed histories of angle of attack, sideslip angle, and Mach number.

Although there were nine pressure taps, in practice not all nine sets of pressure data were necessarily useful. Prior to every test, the taps and sensors were checked and calibrated; nevertheless, problems can and will arise from blasting the test article out of the equivalent of a Howitzer. Sensors, for example, can fail and return unusable data. In these cases, only pressure sensors that returned useful data were included in trajectory reconstruction. Determining which pressure sensors were unusable is relatively straightforward; the most common case of a failed tap resulted in a dead-line pressure reading. The flight parameter estimation method described in this investigation requires a minimum of three pressure taps to compute sideslip, angle of attack, and Mach number. None of the three flights investigated had more than three unusable taps.

6.1 CFD database interpolation

One of the obstacles in using the CFD database was that the data were not cleanly distributed. Instead, there was a certain degree of scatter in all the variables, so that one could not simply collect all index values of Mach 1.60 by looking for $M = 1.60$. There would be values of M = [1.59999, 1.60002, 1.60000, 1.59998 …]. It was necessary to establish a tolerance for every term to account for these variations.

Establishing a pressure model was especially sensitive to this data scatter, with regard to distribution of cone angles. For instance, when attempting to collect C_P values for a cone

angle of 12.59° (where the inner ring of pressure taps are located), looking for index values where $\theta = 12.59°$ will return an empty vector. The reason for this is illustrated in Figure 6.1:

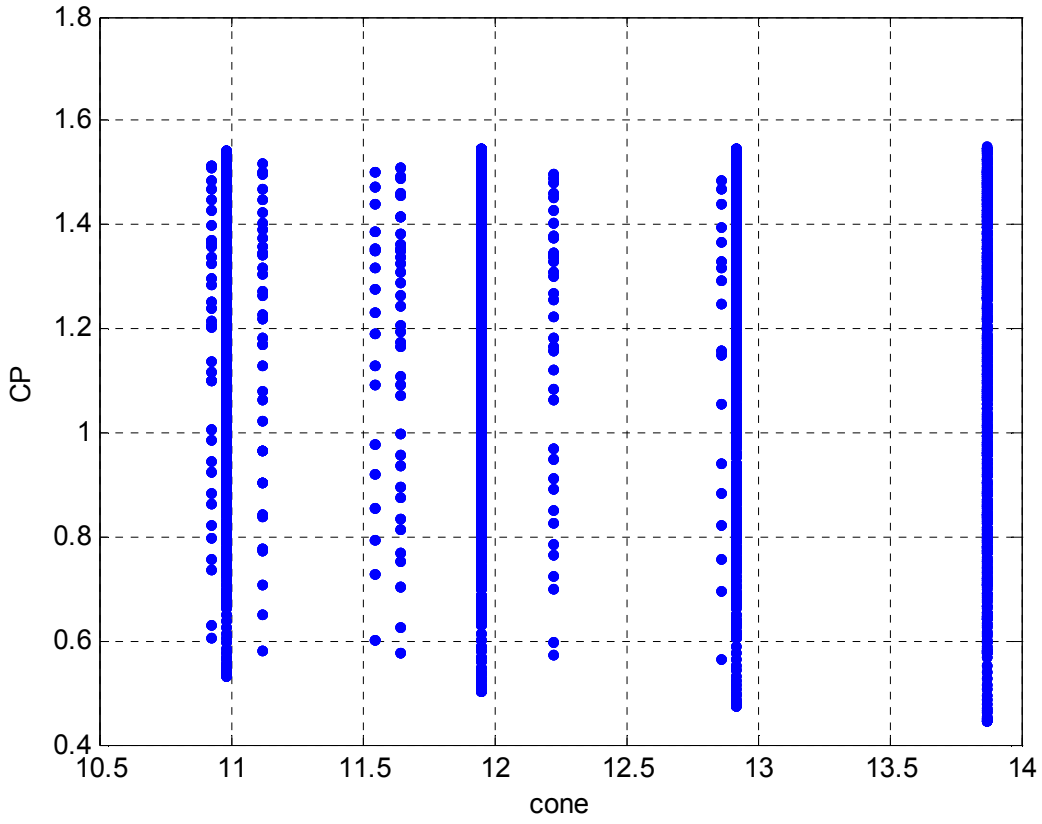

Figure 6.1: CP vs. cone angles near cone = 12.59

There are simply no C_P values at $\theta = 12.59°$ in the CFD database. There are, however, sets of C_P at $\theta = 11.95°$ and 12.91°. In the analysis conducted in (1), a tolerance of 0.45° was set and all coefficients of pressure at 12.59°±0.45° were averaged. For this analysis, an interpolation method will be used to construct a dataset of C_P values at exactly 12.59°.

This is achieved first by filtering out all of the C_P data points except those near the two nearest sets of full data. For $\theta = 12.59°$, these are located at approximately $\theta_1 = 11.95°$ and $\theta_2 = 12.91°$. However, there is even more scatter at these cone angles, despite the seemingly uniform spacing seen in Figure 6.2:

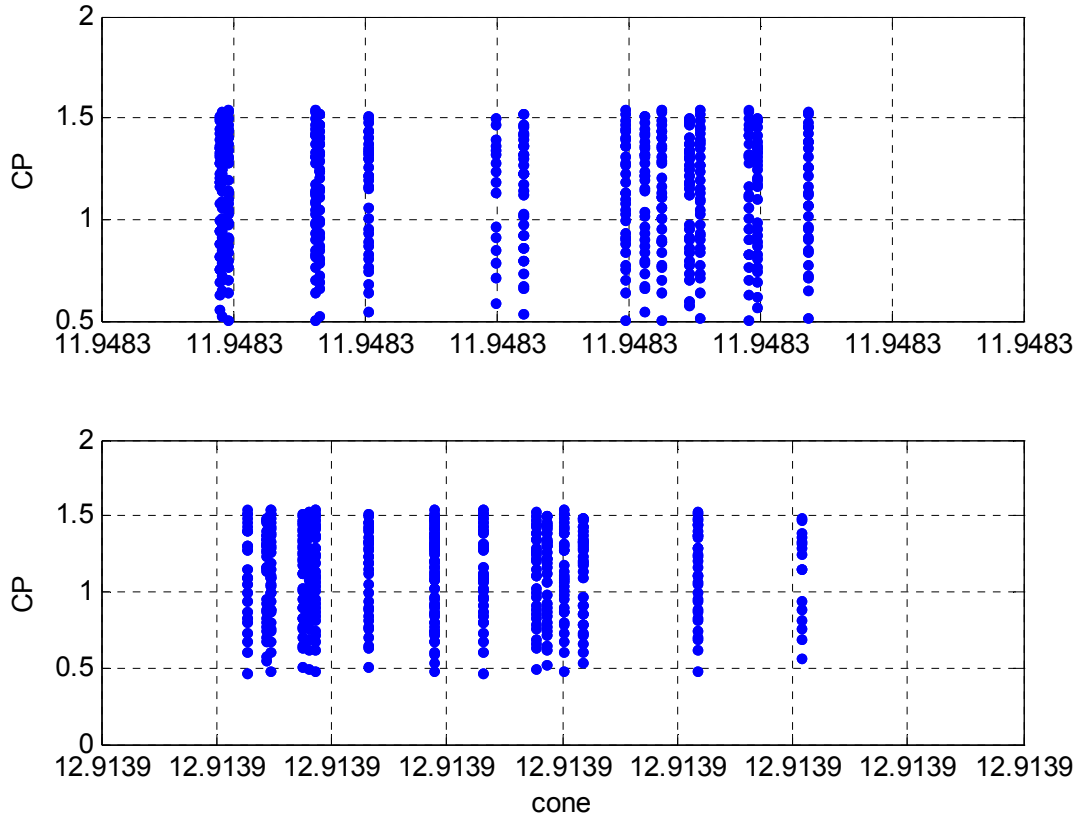

Figure 6.2: Distribution of CFD cone angles near cone = 12.59

For this reason, the values to be interpolated were selected to be near the cone angles of θ_1 and θ_2 listed in Table 5.

Table 5: Cone angles to interpolate and tolerances

	12.59°	**19.45°**	**tolerance**
θ_1	11.94829142°	18.86859280°	1.00E-08°
θ_2	12.91392425°	19.54025391°	1.00E-08°

Because each C_P value at θ_1 corresponded to exactly one C_P value at θ_2, the resultant values were linearly interpolated to get the coefficient of pressure at the desired cone angle.

6.2 CFD pressure distribution

Prior to conducting an analysis of the in-flight pressure behavior, it was helpful to examine the pressure distribution across the surface of the vehicle. As an example, Figure 6.3 illustrates the coefficient of pressure distribution at Mach 1.6, at an angle of attack of 10°.

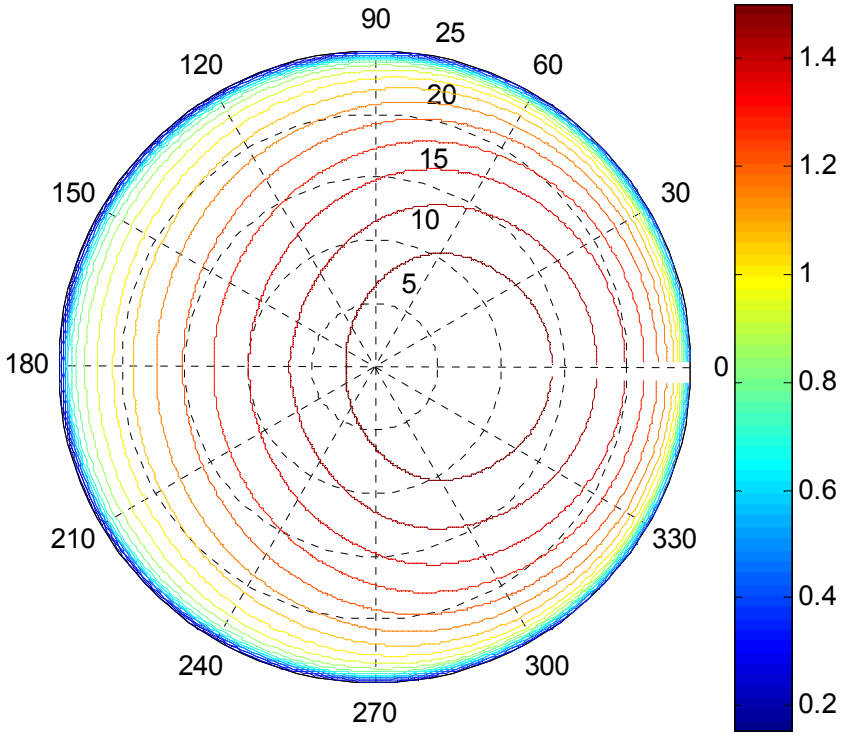

Figure 6.3: CP variation at $M = 1.6$, $\alpha = 10$

Again, because the CFD analysis was conducted with a sideslip angle of zero, the distributions are symmetric along the 0°-180° clock angles. From this Figure, it can be seen that because the angle of attack is low, the stagnation point (where the coefficient of pressure is highest) is close to a cone angle of zero. Indeed, at an angle of attack of zero, it would be expected that the pressure contours would be concentric circles.

At a higher angle of attack, the stagnation point will move along high cone angles. At an angle of attack of 37.5°, the stagnation point lies somewhere between cone angles of 15° and 23°, at a clock angle of zero. This is illustrated in Figure 6.4.

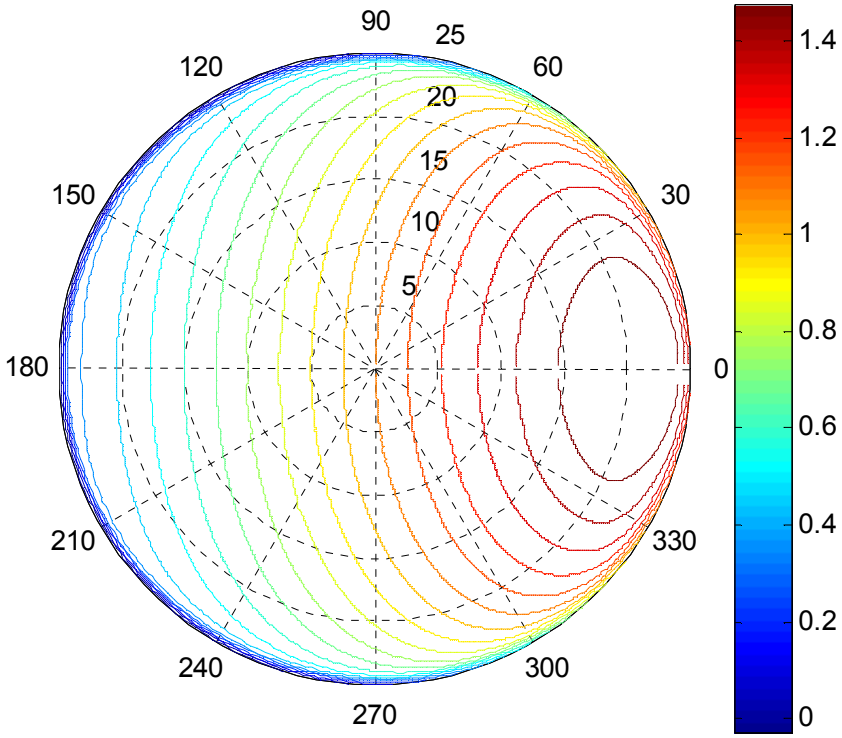

Figure 6.4: CP variation at $M = 1.6$, $\alpha = 37.5$

6.3 Fourier model analysis

In general, the development of the Fourier model is the same as described in (1). However, this document will investigate this development in more detail. A three-term Fourier fit was selected to model the coefficient of pressure as it varied over clock angle:

$$C_P = a_1 + a_2 \cos\phi + a_3 \cos 2\phi$$

where ϕ is the clock angle as defined in Section 2.1. This form was carried over from a previous analysis that concluded higher-order terms were unnecessary (1). At low to medium Mach numbers, from 0.5 to 2.5, this fit was sufficient across all cone angles. From Figure 6.5, it can be seen that the percent error in this regime is well below 1%:

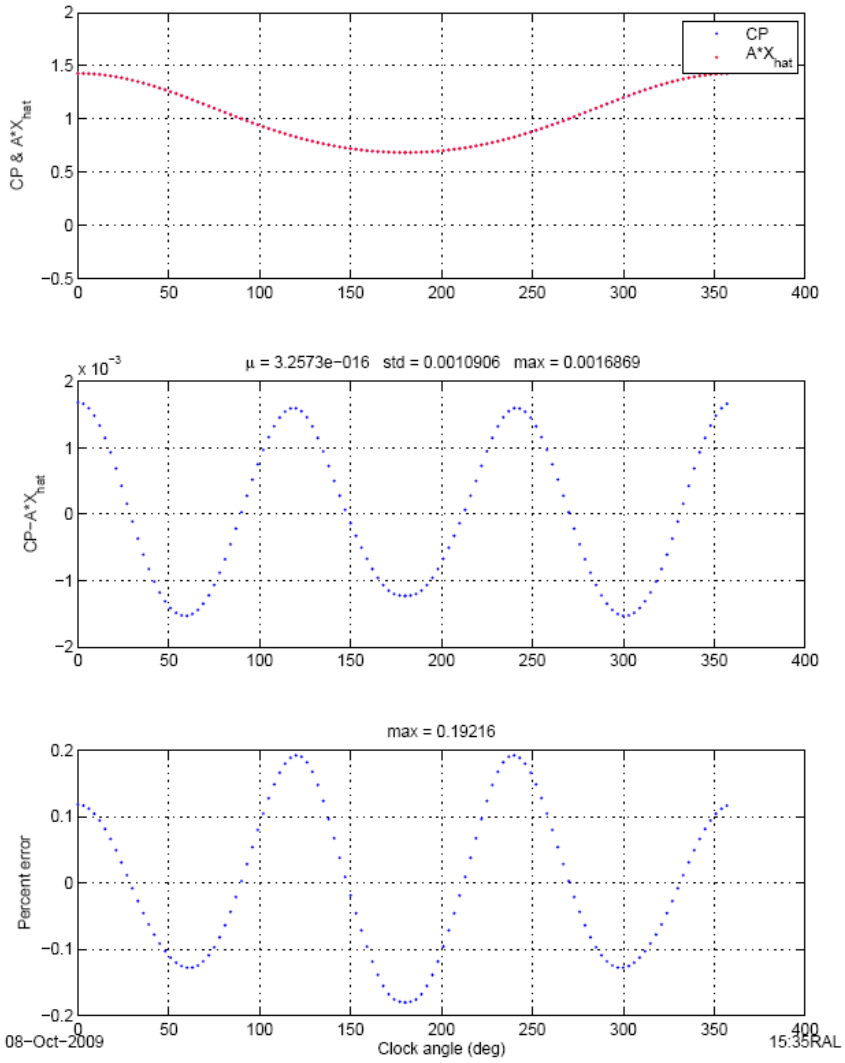

Figure 6.5: CFD and model comparisons, , ,

At Mach numbers of 3 and 4, which were the upper two modeled by CFD, an anomaly was discovered at a clock angle near 50º, at angles of attack near trim. Consider Figure 6.6:

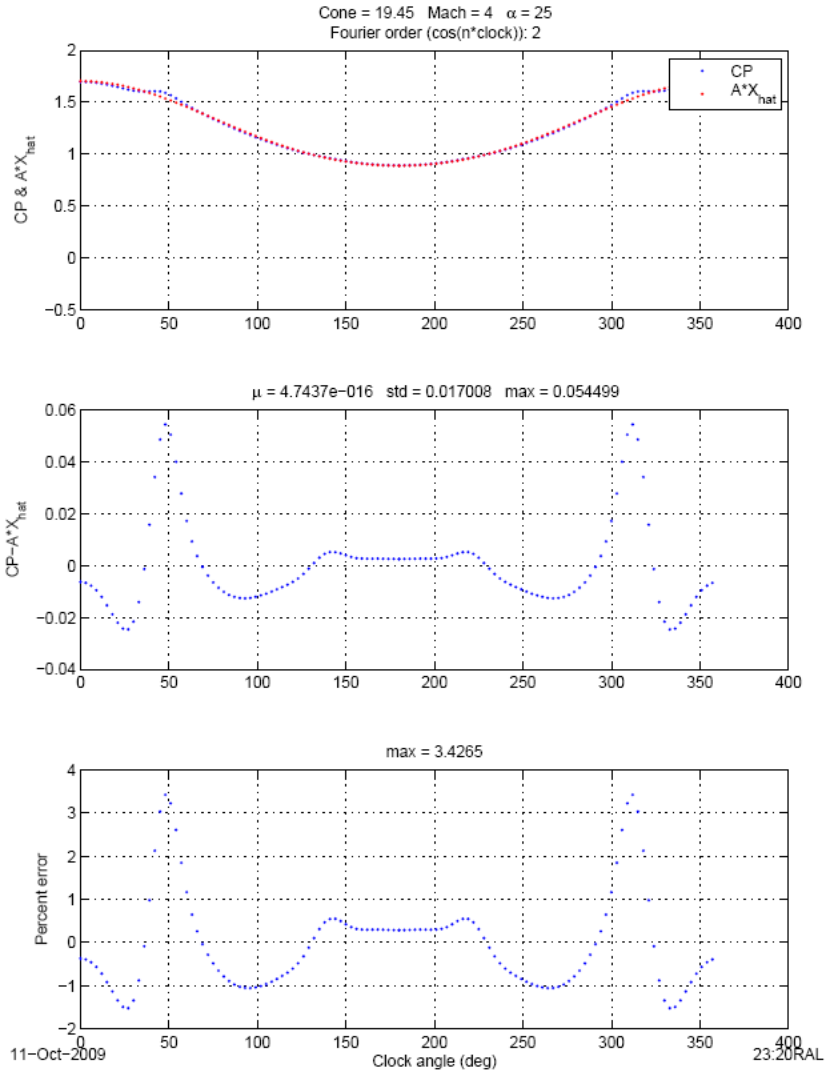

Figure 6.6: CFD and model comparisons, , ,

There is a clear issue at clock angles of 50º and 310º. In the first chart, there is a variation in CP that is not being modeled by the Fourier fit, leading to relatively high percent errors. In this case, the maximum error is 3.4%. Indeed, this is the highest error out of all available angles of attack and Mach numbers. To better characterize this issue, all of the coefficients of pressure were examined near these angles of attack and Mach number.

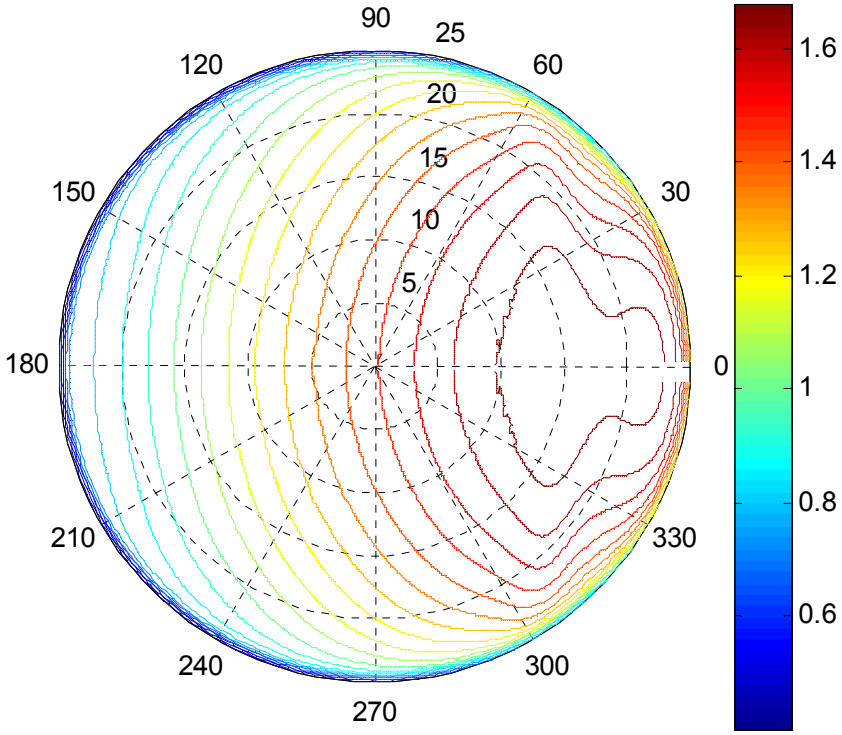

Figure 6.7: CP variation at $M = 4$, $\alpha = 25$

From Figure 6.7, the anomaly can be seen to cover roughly half of the heat shield.

Two possible ways to account for this phenomenon in the model is to increase the number of terms in the Fourier series, or implement a weighting function on the CFD data in areas of high residuals.

6.4 Coefficient of pressure model

As before, it was necessary to compute a coefficient of pressure at a given angle of attack, Mach number, and location on the surface of the vehicle, where $C_P = C_P(\alpha, M, \theta, \phi)$. The script could then loop across all variables. In this case, ϕ is clock angle and θ is cone angle. Given these variables, the appropriate values were extracted from the CFD database. For example, given values of angle of attack, Mach number, and cone angle, the values for the coefficient of pressure can be extracted and plotted against clock angle:

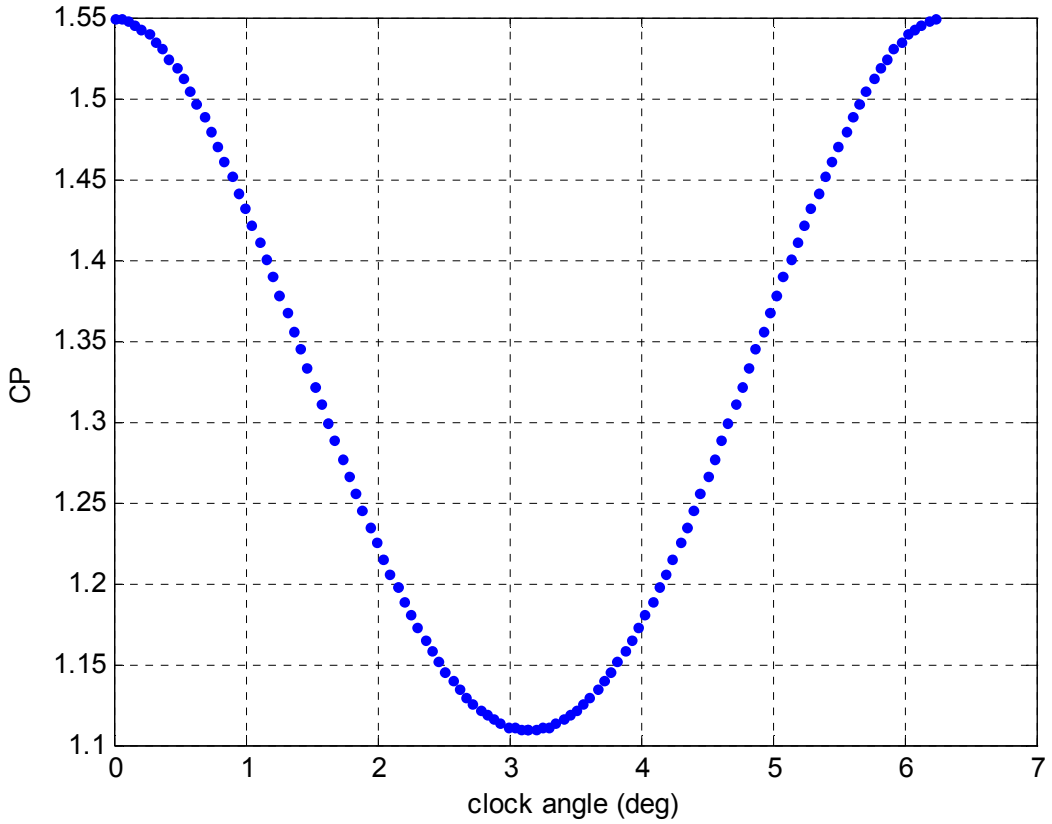

Figure 6.8: Variation of pressure coefficent across clock angle

In this fashion, the pressure across all Mach numbers, angles of attack, and clock and cone angles that are available in the database were computed. However, this in itself did not supply a complete database, because the CFD analysis was conducted only at a particular set of Mach numbers and angles of attack. Although there were multiple clock and cone angles available in the database, the pressures were only computed at the following Mach numbers:

$$M = [0.50\ \ 0.70\ \ 0.90\ \ 0.95\ \ 1.05\ \ 1.10\ \ 1.20\ \ 1.60\ \ 2.00\ \ 2.50\ \ 3.00\ \ 4.00]$$

Compounding the issue was the fact that there were not a set of angles of attack common to all Mach numbers. Collecting all available angles of attack at each Mach number, it can be seen that there is a considerable number of missing angles of attack:

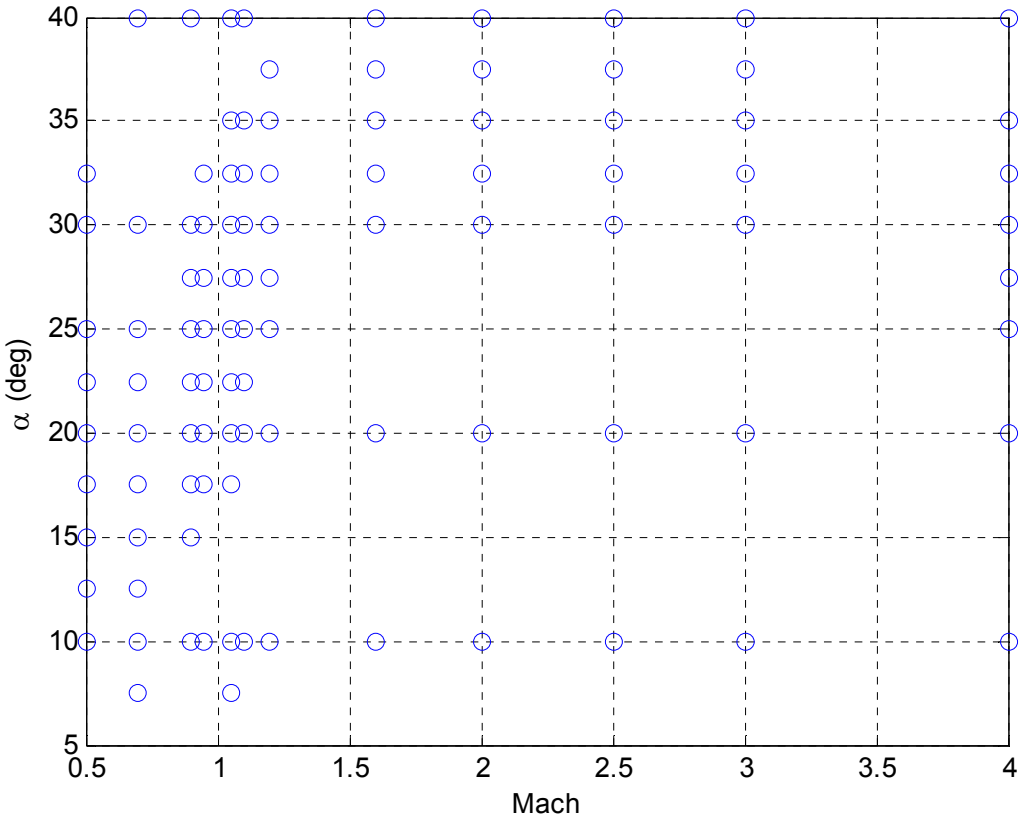

Figure 6.9: Distribution of CFD data at given Mach numbers and angles of attack

To be able to compute the coefficient of pressure at any angle of attack and Mach number within range, it was necessary to interpolate the model coefficients across both the available angles of attack and available Mach numbers. This was achieved by first fitting a second-order polynomial through the Fourier model coefficients across available angles of attack. For example, at M = 1.6, the polynomial fit across the available angles of attack fit to within one percent:

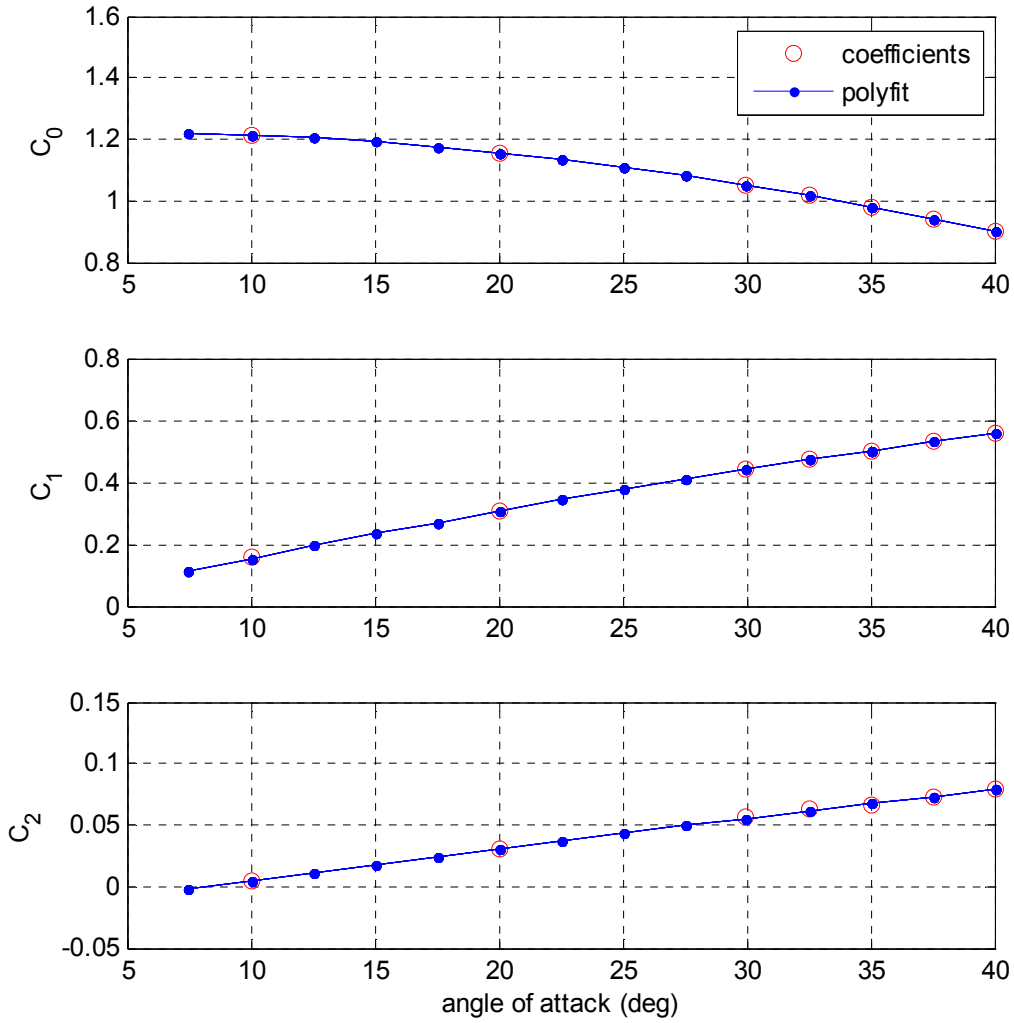

Figure 6.10: Model coefficients for $M = 1.6$, $C_p = c_0 + c_1 \cos\phi + c_2 \cos 2\phi$

Recall the Fourier model $C_P = a_1 + a_2 \cos\phi + a_3 \cos 2\phi$. With the quadratic relation just described, it is possible to write each Fourier model coefficient in terms of angle of attack:

$$a_1 = c_1 + c_2\alpha_T + c_3\alpha_T^2$$

$$a_2 = c_4 + c_5\alpha_T + c_6\alpha_T^2$$

$$a_3 = c_7 + c_8\alpha_T + c_9\alpha_T^2$$

Note that the angles of attack are labeled as total angle of attack because the CFD analysis was conducted at a sideslip angle of zero. It is therefore necessary to ensure that at

$\alpha_T = 0$, C_P has no clock angle dependency; that is, $C_P = c_1$. To do this, the coefficients c_4 and c_7 are set to zero. The coefficient of pressure can then be described by a seven-term model (note that the coefficients have been re-numbered to account for the removal of c_4 and c_7):

$$C_P = (c_1 + c_2\alpha_T + c_3\alpha_T^2) + (c_4\alpha_T + c_5\alpha_T^2)\cos\phi + (c_6\alpha_T + c_7\alpha_T^2)\cos 2\phi$$

The CFD model was adjusted to fit the wind-tunnel data, which is given more credence. The following equation, describing this adjustment, is reproduced for clarity (1 p. 52):

$$\{c_1 \quad \cdots \quad c_7\} = \{c_1 \quad \cdots \quad c_7\}_{CFD} + \begin{bmatrix} \frac{\partial C_{P,model}}{\partial c_1} & \cdots & \frac{\partial C_{P,model}}{\partial c_7} \\ \vdots & \vdots & \vdots \end{bmatrix} \begin{Bmatrix} C_{P,WTT} - C_{P,CFD} \\ \vdots \end{Bmatrix}$$

With this, it was finally possible to compute the actual pressure at the given state, using global constants of atmospheric pressure P_∞ and heat capacity ratio γ:

$$P = \frac{1}{2}P_\infty(2 + \gamma C_P M^2)$$

This equation was developed by Sebastian (1 p. 53).

6.5 Pressure model coefficients

The original pressure model by Sebastian included only two coefficients, a bias and a scale factor. An investigation of the trends in the residuals resulted in computing two additional terms, due to the presence of quadratic and cubic trend lines remaining in these residuals. The improvement of these residuals is shown in Section 7.4. The final pressure model was therefore of the form

$$P_{com} = c_1 + c_2 P_{mod} + c_3 P_{mod}^2 + c_4 P_{mod}^3$$

where c_1 is the bias, c_2 is the scale factor, c_3 is the quadratic coefficient, and c_4 is the cubic coefficient.

7 Flight Parameter Estimation

Given a set of pressure readings from the onboard pressure transducers, the set of flight parameters described in Section 2.2 can be estimated using a least-squares approach. This method computes a solution with the minimum error between the observed and computed pressures. Specifically, a minimum variance approach with differential correction and a priori was used to estimate the flight parameters.

7.1 Overview of flight parameter estimation

For clarity, define the number of observed data points across time as n. Thus, the observed data can be arranged as an [n x 9] array:

$$P_{obs}(t_{1..n}) = \begin{bmatrix} P_1(t_1) & \cdots & P_9(t_1) \\ \vdots & \vdots & \vdots \\ P_1(t_n) & \cdots & P_9(t_n) \end{bmatrix}$$

As an example, the pressure data from PTM-02 is shown in Figure 7.1.

The flight parameters Mach number M, angle of attack α, and sideslip angle β, being functions of pressure, change at every time step and are defined as *local parameters*. The *global parameters* of bias, scale factor, and quadratic and cubic terms, apply to the entire dataset. Thus, in the most general sense, the global parameters are calculated after the local parameters are computed at each time step.

More specifically, there are two loops in the estimation software, an inner and outer loop. Within the outer loop is the inner loop, where the software processes every data point across time and computes the local parameters. When the inner loop has finished processing the data, the outer loop computes the global parameters. The estimates are updated and checked for convergence; if the convergence criteria are not met, the outer loop begins again and executes the inner loop. This process is illustrated as a flowchart in Figure 7.2.

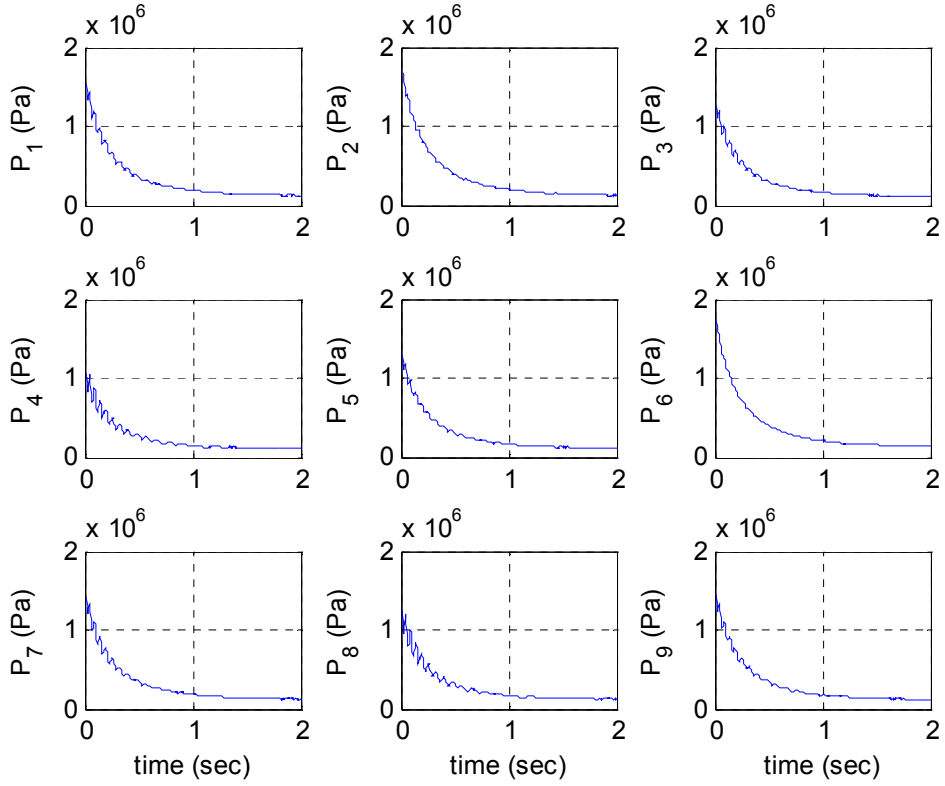

Figure 7.1: Pressure transducer readings from PTM-02

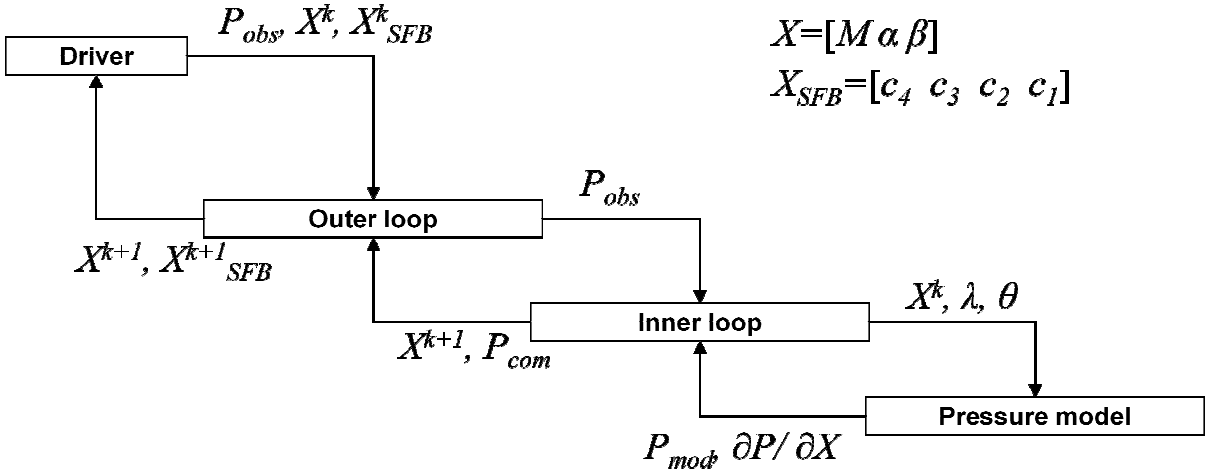

Figure 7.2: Diagram of inner and outer loop logic flow ([k] denotes current estimate, [k+1] denotes new estimate)

7.2 Minimum variance estimation

Both the inner and outer loops compute an estimate by utilizing the estimation method of minimum variance. In batch linear, unbiased minimum variance, the estimated value $\hat{\mathbf{x}}$ is computed by the equation

$$\hat{\mathbf{x}} = (\mathrm{A}^{\mathrm{T}}\Gamma_{\varepsilon}^{-1}\mathrm{A})^{-1}\mathrm{A}^{\mathrm{T}}\Gamma_{\varepsilon}^{-1}\mathbf{y}$$

where $\mathbf{y}$ is the vector of observations and A is the sensitivity matrix (7 pp. 8.12-3). The associated covariance, which directly relates the accuracy of the estimate with the accuracy of the observations, is

$$\Gamma_{\mathrm{x}} = (\mathrm{A}^{\mathrm{T}}\Gamma_{\varepsilon}^{-1}\mathrm{A})^{-1}$$

7.2.1 Differential correction with a priori

With highly non-linear problems, such as the estimation of the flight parameters from pressure data, it is advantageous to use a differential correction approach with a priori. This method incrementally adjusts the estimates and uses prior knowledge to efficiently compute the new estimate. With a priori and differential correction, the minimum variance estimator becomes

$$\delta\hat{\mathbf{x}}_k = \left(\mathrm{A}^{\mathrm{T}}\Gamma_{\varepsilon}^{-1}\mathrm{A} + \Gamma_{\mu}^{-1}\right)^{-1}\left(\mathrm{A}^{\mathrm{T}}\Gamma_{\varepsilon}^{-1}\mathbf{y} + \Gamma_{\mu}^{-1}(\mu - \mathbf{x}_k)\right)$$

where $\hat{\mathbf{x}}_{k+1} = \hat{\mathbf{x}}_k + \delta\hat{\mathbf{x}}_k$ provides the estimate update. In this case, $\mathbf{y}$ is the vector of the difference between observed and computed data, and μ is the a priori. The covariance of the final estimate is

$$\Gamma_{\mathrm{x}} = \mathrm{V}(\hat{\mathbf{x}} - \mathbf{x}) = \left(\mathrm{A}^{\mathrm{T}}\Gamma_{\varepsilon}^{-1}\mathrm{A} + \Gamma_{\mu}^{-1}\right)^{-1}$$

7.2.2 Application to pressure-based solution

Since there are two loops, there are two sets of estimates. The inner loop estimates the flight parameters:

$$\hat{\mathbf{x}}_{inner} = [M \quad \alpha \quad \beta]^T$$

The outer loop estimates the coefficients of the pressure model for all nine taps at once:

$$\hat{\mathbf{x}}_{outer} = [[c_4] \quad [c_3] \quad [c_2] \quad [c_1]]^T$$

where $[c_1]$ is the vector of nine biases, $[c_2]$ is the vector of nine scale factors, $[c_3]$ is the vector of nine quadratic coefficients, and $[c_4]$ is the vector of nine cubic coefficients. These coefficients are applied to the modeled pressure data for each tap. For example, for tap 5, the computed pressure would be

$$P_{5,com} = c_1(5) + c_2(5)P_{5,mod} + c_3(5)P_{5,mod}^2 + c_4(5)P_{5,mod}^3$$

It is the difference between this computed pressure and the observed pressure that the minimum variance method attempts to minimize.

7.3 Pressure-derived flight parameters

The flight parameters derived from the pressure data using the methods described above are shown in Figure 7.3.

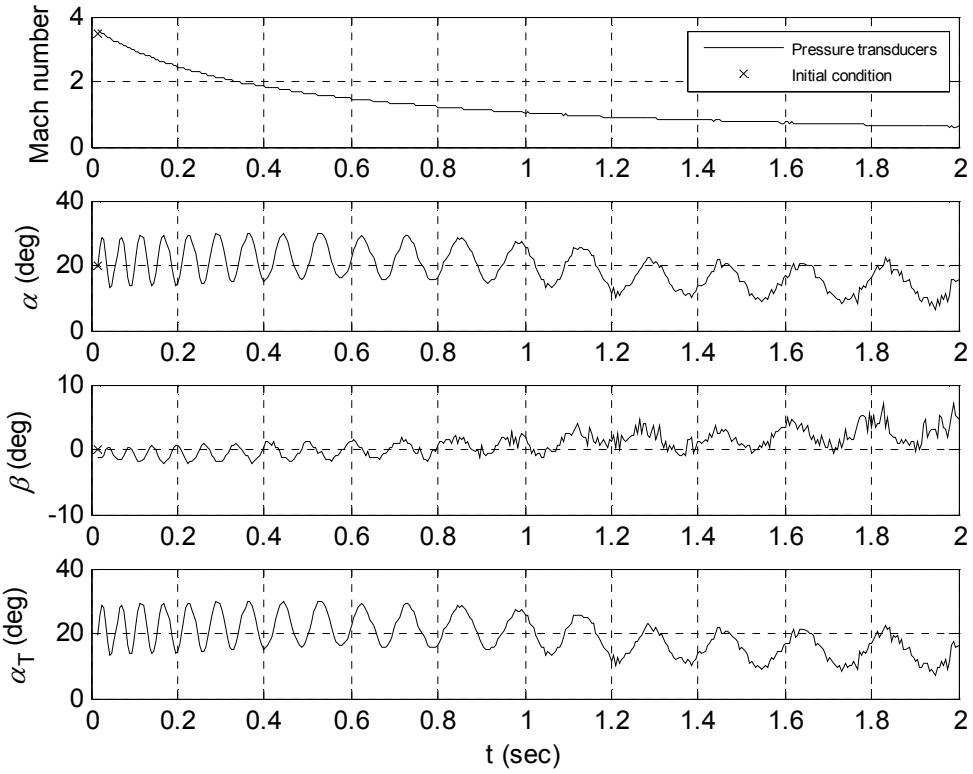

Figure 7.3: Pressure-derived flight parameters, PTM-02

When compared to the IMU-based flight parameters in Figure 5.4, these angles are much more reasonable. It is important to note that the sideslip angle β is small compared to the angle of attack α; in fact, total angle of attack $T$is essentially α. The significance of this will become more apparent in the statistical analysis in Chapter 8. For reference, the converged flight parameters for all three flights are presented in Figure 7.4.

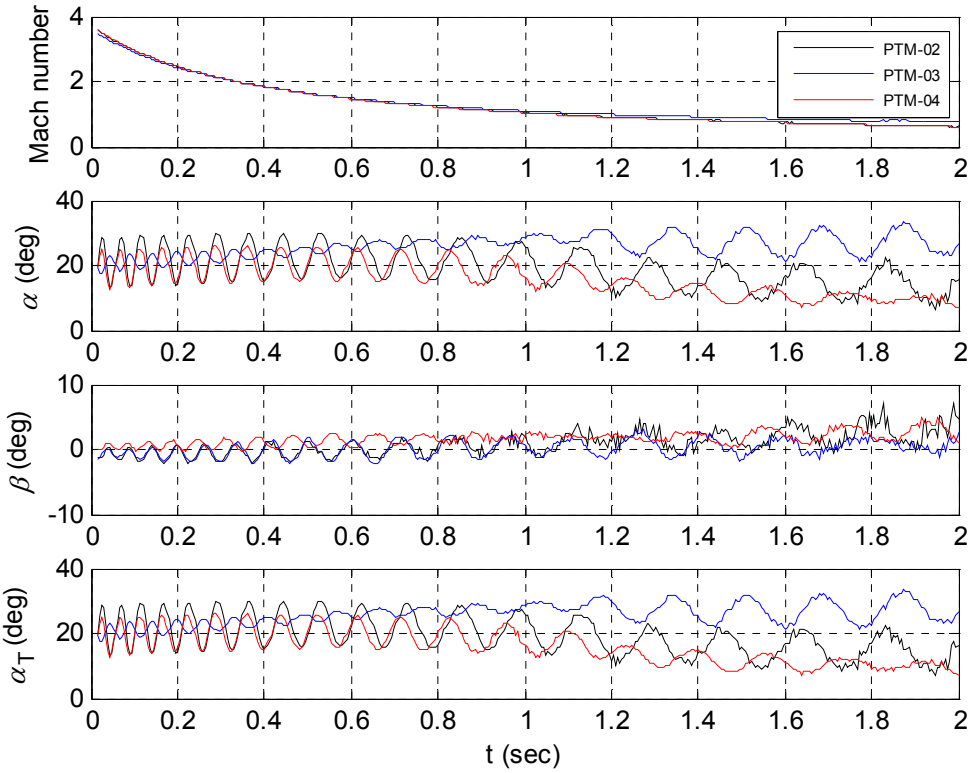

Figure 7.4: Pressure-derived flight parameters, PTM-02, -03, -04

7.4 Analysis of pressure residuals

It is useful to examine the residuals between the observed pressures and the final, converged computed pressures, as trends and anomalies can often be detected in such data. As discussed in Section 6.5, the residuals were significantly improved by moving from a linear model to a cubic model. Figure 7.5 and Figure 7.6 show the residuals between the observed and computed pressures using the linear and cubic models, respectively.

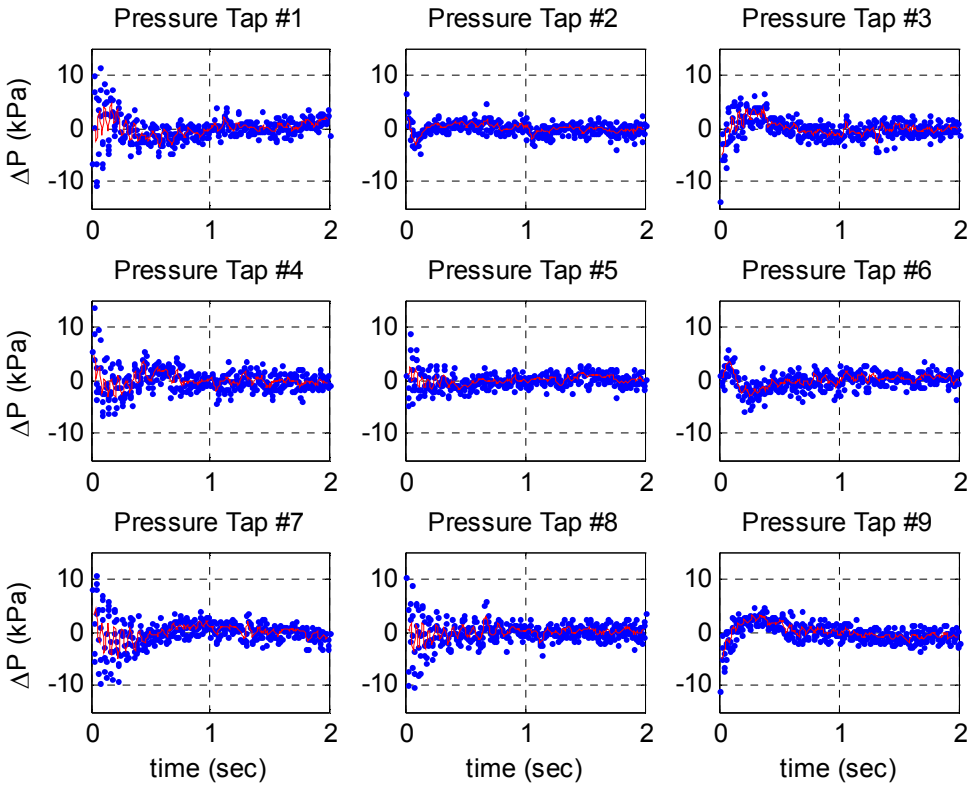

Figure 7.5: Pressure residuals, linear model, PTM-02

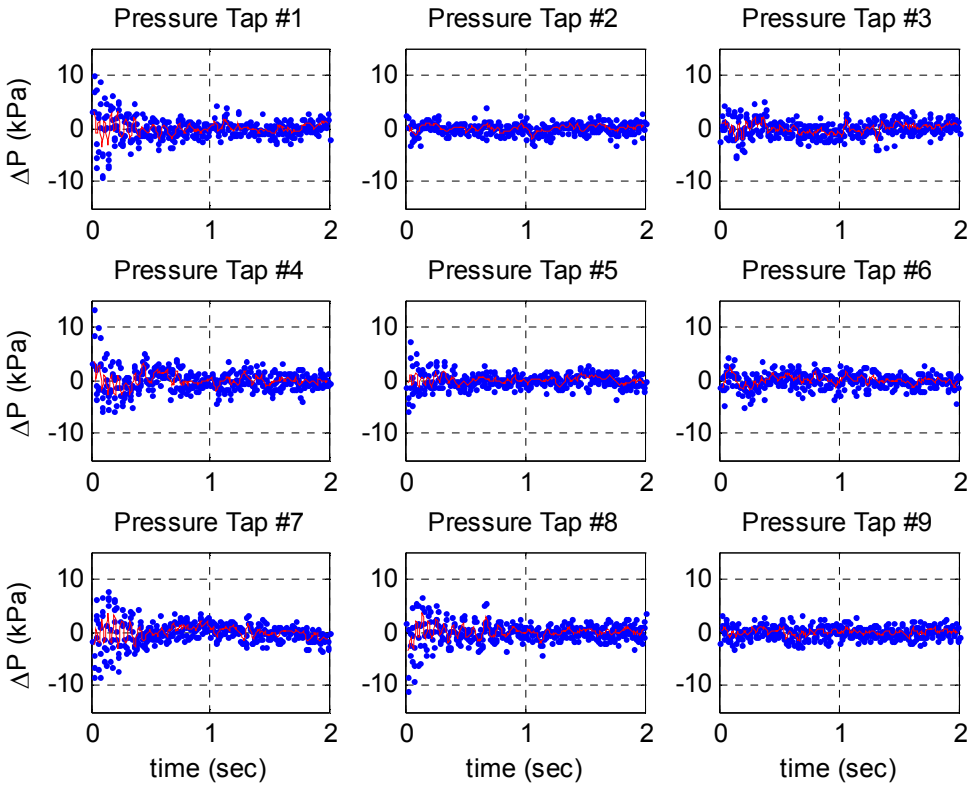

Figure 7.6: Pressure residuals, cubic model, PTM-02

Table 6: Pressure model coefficients, cubic model, PTM-02

Tap	Cubic	Quadratic	Scale Factor	Bias (Pa)
1	-2.955E-14	6.210E-08	0.962	-1827
2	1.044E-14	-2.297E-08	1.017	1266
3	-2.136E-14	1.998E-08	1.017	-5410
4	2.673E-14	-4.168E-08	1.055	-2470
5	-6.184E-15	1.641E-08	0.994	903
6	-7.843E-15	2.432E-08	0.979	5202
7	1.481E-14	-1.908E-08	0.985	2727
8	2.790E-14	-4.028E-08	0.998	6869
9	-1.606E-15	-1.186E-08	1.012	-6032

From these figures, it can be seen that the long-term trends have been essentially removed. However, there is still a high-frequency signal present in some of the taps that matches the period of angle of attack, meaning that the model is under- or overestimating the

pressures, depending on the tap. Several possibilities for the source of this signal exist, including unexpected CFD behavior at high Mach numbers (see Section 6.3), sensors not being calibrated as high as flight pressures, and tap location uncertainty. But perhaps the most likely explanation for the signal still present in the residuals is the pressure differential across the tap.

The diameter of each pressure tap is 0.040 inches. By looking at CFD data, the amount of pressure change across the vertical taps (taps 1, 2, 4, 6, and 8) can be found, and are presented in Table 7. A diagram of the cross-section of a pressure tap is shown in Figure 3.6.

Table 7: Pressure differential across tap (Pascals)

Cone angle	**M = 4 α = 30**	**M = 4 α = 25**	**M = 4 α = 20**	**M = 3 α = 30**	**M = 3 α = 25**	**M = 3 α = 20**
-19.45	11487	12134	12438	6237	6500	6635
-12.59	10975	11184	11037	6202	6253	6100
19.45	846	1527	7764	2045	3567	5544
12.59	7442	5293	6710	3763	2799	2082

From the table, it can be seen that the pressure differential across a single tap can be as high as 12 kPa, whereas from Figure 7.6, the maximum amplitude of the residuals is approximately 10 kPa. Clearly, this is an issue, since there is no way to estimate which pressure across this differential that the transducer is measuring.

At present, there is no single definitive explanation for the signal in the pressure residuals.

8 Statistical Analysis

A statistical analysis of the results obtained through the parameter estimation was conducted. The goal was to compute the uncertainties associated with the estimation of the flight parameters.

8.1 Consider parameters

The uncertainties computed in the minimum variance process described in Section 7.2 are the noise-only uncertainties, that is, they are the uncertainties associated with the accuracy of the observations. Of course, there is more than simply noise in the data, so it is necessary to account for other factors that may have affected the solution. In this analysis, the estimation of the global parameters is "considered," and its effects on the estimation uncertainty are computed. Specifically, the expected value of the estimator is

$$\mathrm{E}(\hat{\mathbf{x}}) = \mathbf{x} + (\mathrm{A}^{\mathrm{T}}\Gamma_{\varepsilon}^{-1}\mathrm{A})^{-1}\mathrm{A}^{\mathrm{T}}\Gamma_{\varepsilon}^{-1}\mathrm{B}\mu_{\mathrm{z}}$$

where μ_{z} is the mean value of the parameter being considered. In terms of the pressure estimation software, the matrix B is the sensitivity matrix from the inner loop, and A is the sensitivity matrix from the outer loop. The second term in the equation is the bias added to the original estimate from the new parameters being considered. Similarly, the new covariance is defined as

$$\Gamma_{\mathrm{x}} = \mathrm{V}(\hat{\mathbf{x}} - \mathbf{x}) = (\mathrm{A}^{\mathrm{T}}\Gamma_{\varepsilon}^{-1}\mathrm{A})^{-1} + (\mathrm{A}^{\mathrm{T}}\Gamma_{\varepsilon}^{-1}\mathrm{A})^{-1}\mathrm{A}^{\mathrm{T}}\Gamma_{\varepsilon}^{-1}\mathrm{B}\Gamma_{\mathrm{z}}\mathrm{B}^{\mathrm{T}}\Gamma_{\varepsilon}^{-1}\mathrm{A}(\mathrm{A}^{\mathrm{T}}\Gamma_{\varepsilon}^{-1}\mathrm{A})^{-1}$$

In this equation, the first term is the noise-only covariance as before. Thus, the second term is how much the parameters being considered are affecting the uncertainty.

8.2 Uncertainties

The original, noise-only uncertainties are shown in Figure 8.2. An examination of the root-mean-square (RMS) of the pressure residuals, however, indicated that an adjustment of the uncertainties was necessary in the upper Mach number regime. The RMS of the residuals is shown in Figure 8.1.

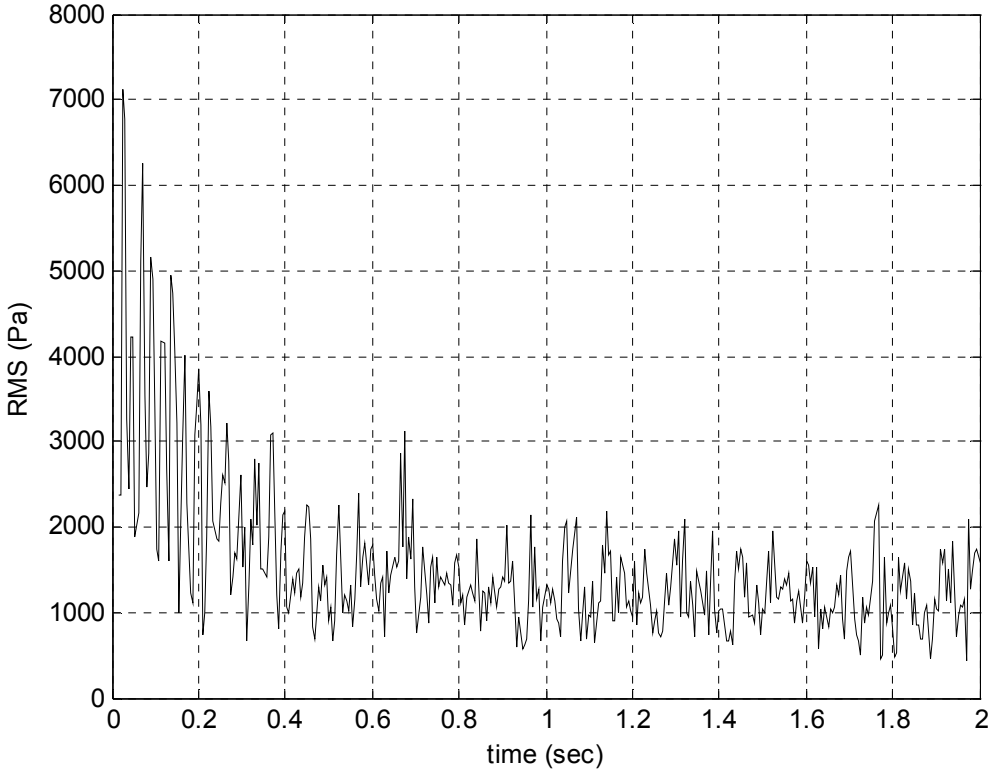

Figure 8.1: RMS of pressure residuals

The first 0.6 seconds of the uncertainties where inflated using an equation that was derived empirically from the RMS curve:

$$\sigma_{t=0.0..0.6s} = \sigma_{t=0.0..0.6s} \times 12000e^{\frac{-2.3t}{3000}}$$

The uncertainties of the estimated flight parameters are shown in Figure 8.2, along with the inflated noise-only uncertainties and the consider parameter uncertainties. Figure 8.3 shows the consider parameter uncertainties from Figure 8.2 in error-bar format. Note that on the scale of the plot, the error on Mach number is nearly indiscernible.

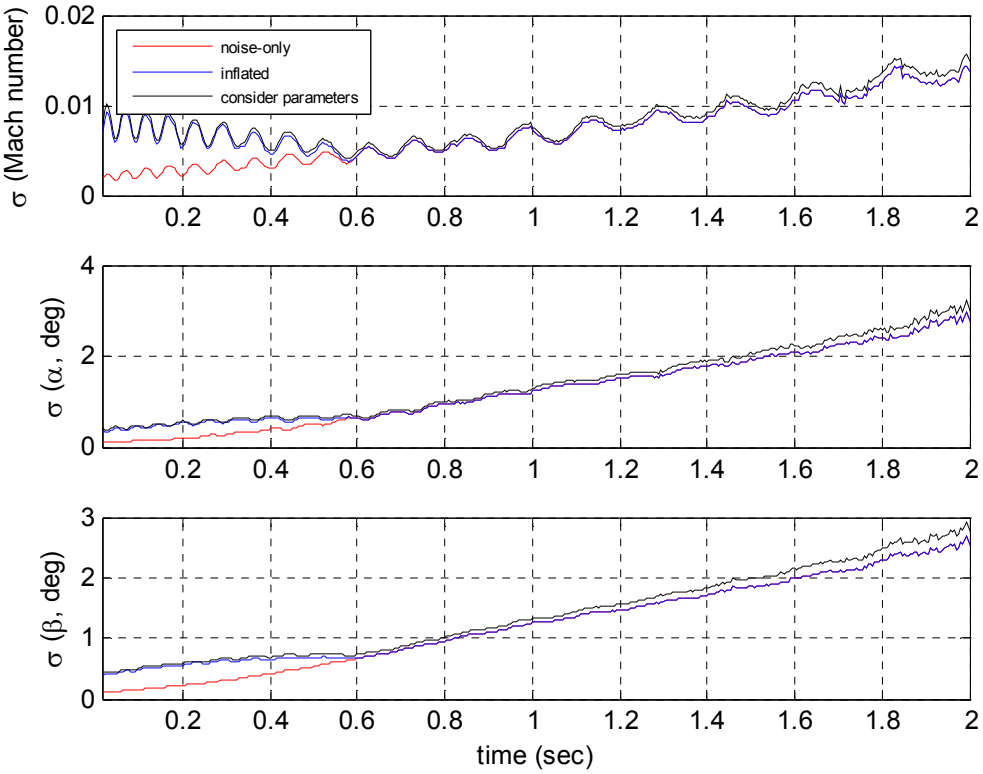

Figure 8.2: PTM-02 uncertainties

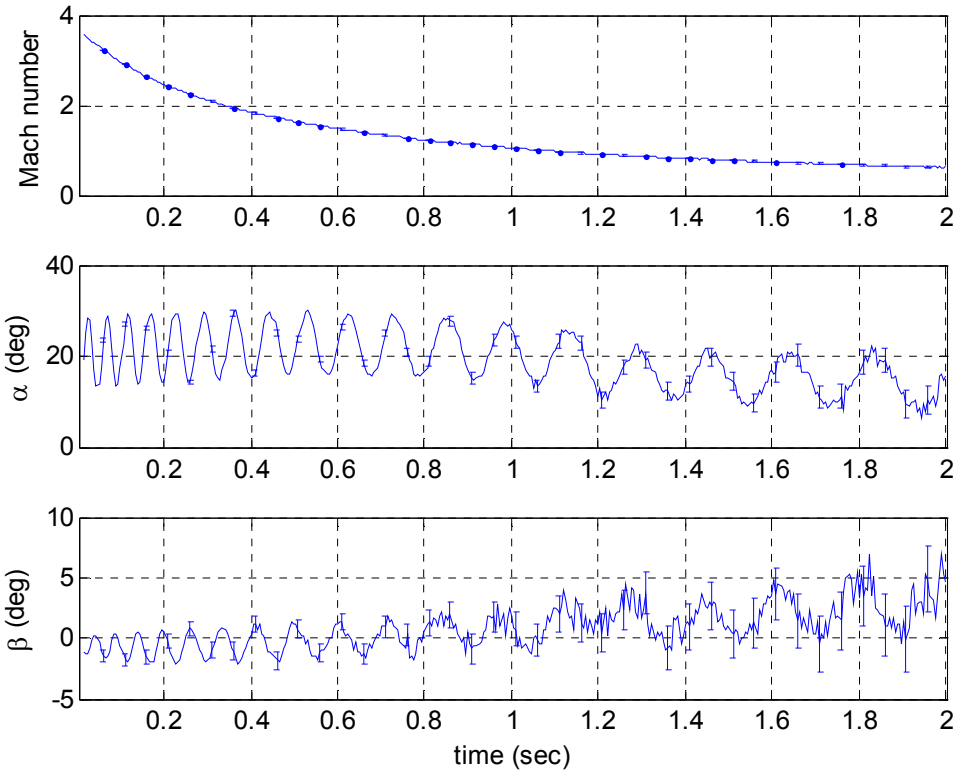

Figure 8.3: Error bars for flight parameters, PTM-02

8.3 Verification of uncertainties

Consider again the equation for the expected value of the estimator:

$$E(\hat{\mathbf{x}}) = \mathbf{x} + (A^T \Gamma_\varepsilon^{-1} A)^{-1} A^T \Gamma_\varepsilon^{-1} B \mu_z$$

It is possible to numerically verify the bias term on the right-hand side of the equation by emulating the consider parameters approach. For each tap, the bias, scale factor, and nonlinear terms were manually perturbed one by one, and a pressure solution was found with this perturbed parameter. The results were various sets of flight parameters, each of which corresponded to a perturbed bias, scale factor, or nonlinear term on a single tap.

For example, for one run the bias on tap 1 was perturbed by 5000 Pa. Thus, the flight parameter solution corresponded to a pressure data set where tap 1 was biased by 5000 Pa. This was repeated for all taps and all coefficients. Figure 8.4 shows the effects on the solutions after biasing each tap. As expected, perturbing the taps nearest to the stagnation

point (taps 2 and 6) yield the highest changes in the solutions. It is also worth noting that with respect to β, biasing tap 3 has the opposite effect of biasing tap 5, which is to be expected as the taps along the horizontal axis define the sideslip.

Similarly, Figure 8.5 shows the effects on the solutions after perturbing the quadratic terms on each tap. Again as expected, the taps nearest to the stagnation point show the greatest effects. Additionally, the effects are greater in the higher Mach regime, as the quadratic term is being squared.

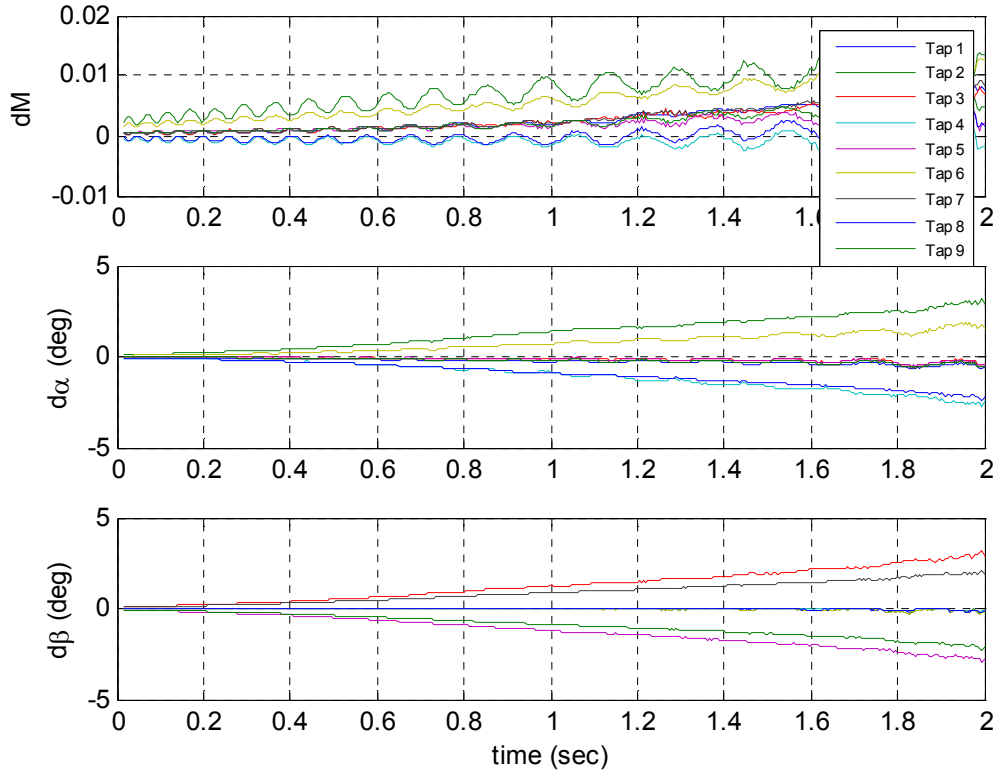

Figure 8.4: Effect of +5000 Pa bias on estimated flight parameters

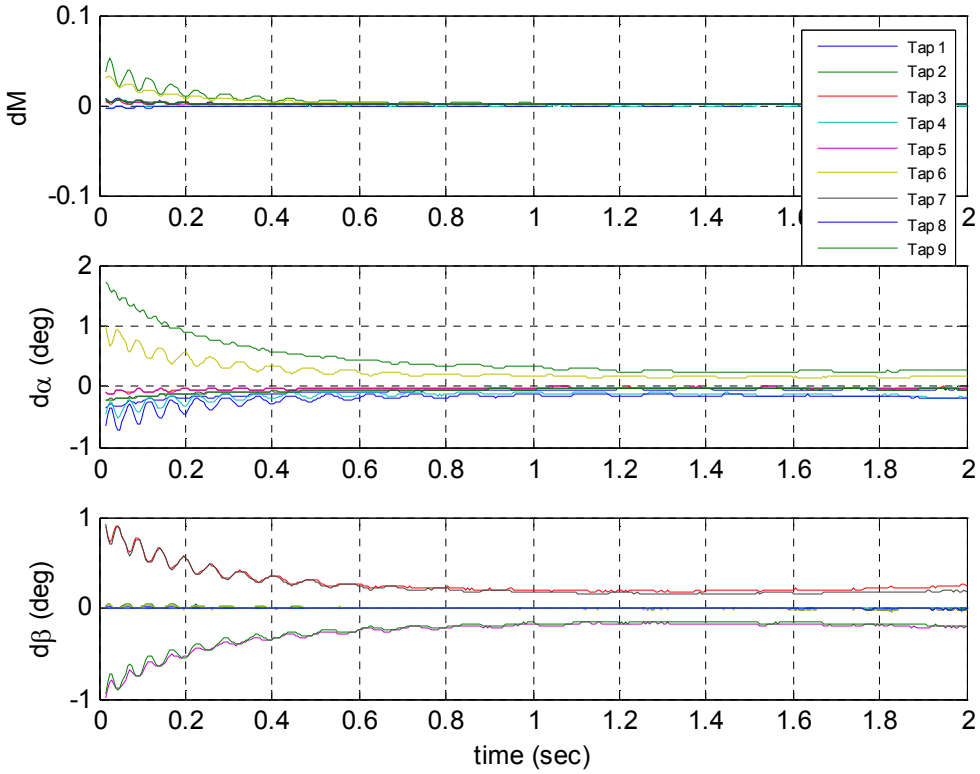

Figure 8.5: Effect of +3E-8 perturbation on quadratic term on estimated flight parameters

The bias term on the right-hand side of the equation is essentially equivalent to the biases computed using the method just described. By setting the mean value of the consider parameter μ_z to the same values used in the previous method (for example, a 5000 Pa perturbation for bias and +3E-8 for the quadratic term), the two biases can be compared.

Figure 8.6 shows a comparison of the biases when the bias terms on the taps are perturbed. Similarly, Figure 8.7 shows a comparison of the biases when the scale factors on the taps are perturbed. The two sets of curves match in trends and magnitude, which is a validation of the consider parameters approach. This also implies that the linear assumption made in the consider parameters method is valid.

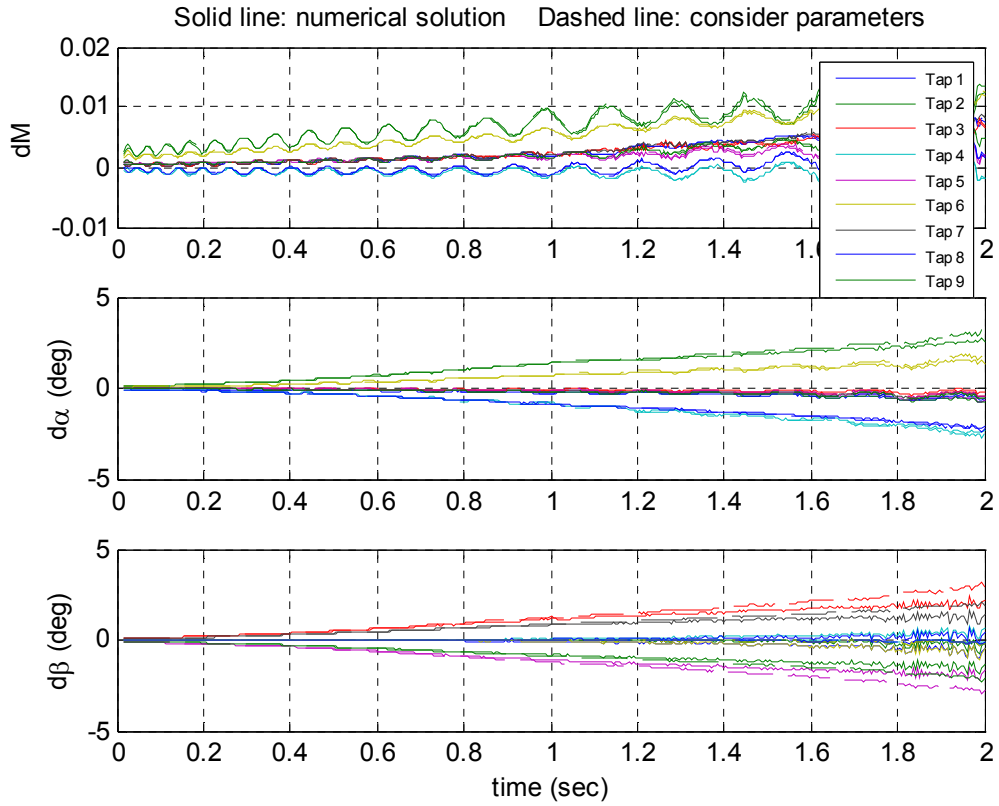

Figure 8.6: Comparison of numerical and consider parameter methods to computing biases on flight parameters, +5000 Pa perturbation to bias term

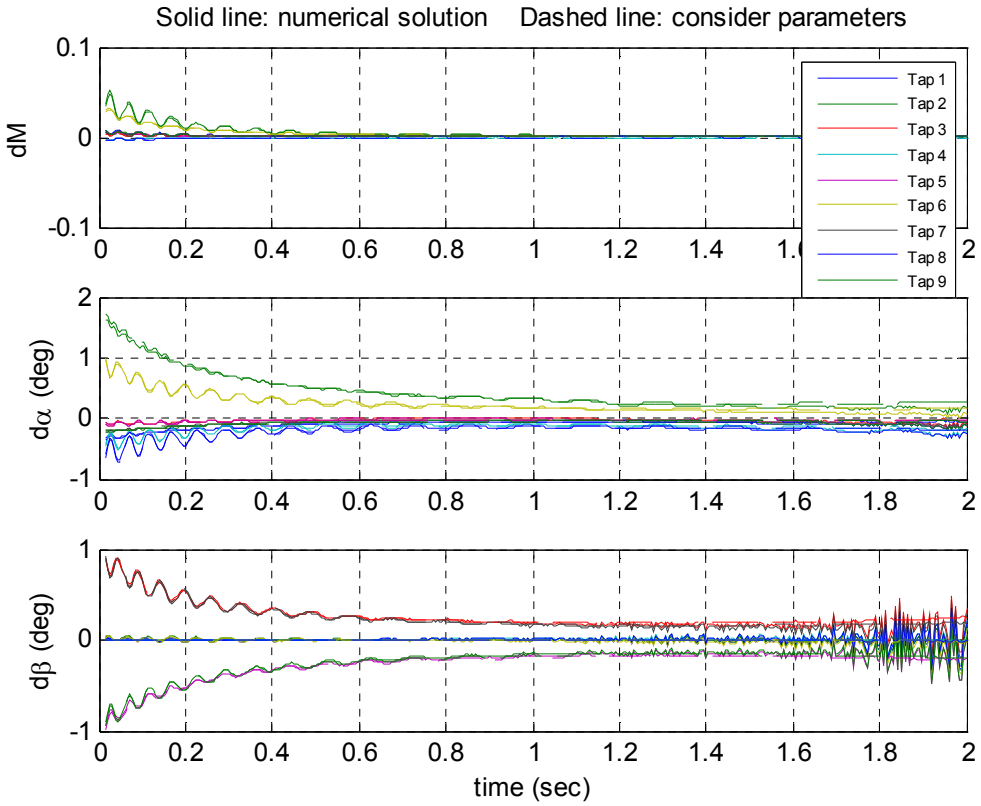

Figure 8.7: Comparison of numerical and consider parameter methods to computing biases on flight parameters, +3E -8 perturbation to quadratic term

Part IV: Summary and Conclusions

9 Conclusions

This thesis presented two major methods of reconstructing the flight parameters of Mach number, angle of attack, and sideslip angle. The first method, which utilized radar and the inertial measurement unit aboard the flight vehicle, was investigated in Part II. The second method, which reconstructed the parameters solely from pressure data, was investigated in Part III.

9.1 Methods of reconstruction

The IMU reconstruction method could only qualitatively verify the trajectory, due to various problems encountered with the sensors and data. Similarly, the radar-based reconstructions of the flight angles could verify long-term trends, but did not offer sufficient fidelity to verify the amplitudes from the pressure-based method.

The pressure-based reconstruction yielded flight parameters that were reasonably close to the expected behavior. Mach number in particular was well-established, as it was verified to within 0.002 of radar Mach number.

Fortunately, the amplitudes of the pressure-based flight angles could be verified from other sources. Specifically, the time-derivatives of the flight angles matched reasonably well with the magnetometer-derived body rates. Thus, the pressure-based flight parameters of Mach number, angle of attack, and sideslip angle could be verified from data sources that were totally independent of the pressure transducers.

9.2 Unresolved issues

The sensors in the inertial measurement unit had several problems that led to difficulty in finding a reliable IMU-based trajectory. Rate sensors appeared to have acceleration biases, accelerometers appeared to have misalignments, and magnetometers measured a variable magnetic field strength throughout the flight. In addition, all of the

sensors encountered a lag after launch, forcing the reconstruction to begin at time 0.15s instead of time zero. All of these issues prevented an accurate IMU-based flight parameter reconstruction.

With regards to the pressure data, fewer issues were encountered, aside from faulty or failed pressure transducers. Perhaps the most significant issue was the high-frequency signals still present in the residuals, and work is still ongoing to resolve this inconsistency.

9.3 Future work and applications

The reconstruction and verification methods described in this thesis are by no means definitive. Further applications include utilizing these methods on other entry vehicles, such as Mars Science Lab (currently scheduled to be launched in 2012). This is particularly intriguing, as this would involve applying the pressure-based reconstruction to a vehicle that is traveling through the Mars atmosphere, which is not as well-established as that of Earth's. Clearly, there is a need for further investigation.

References

1. **Sebastian, Thomas.** *Methods for the Determination of Aerodynamic Parameters and Trajectory Reconstruction of the Orion Command Module from Scale Model Aeroballistic Flight Data.* Department of Mechanical & Aerospace Engineering, North Carolina State University. Raleigh : NC State University, 2008. Master's Thesis.

2. **Duke, Eugene L., Antoniewicz, Robert F. and Krambeer, Keith D.** *Derivation and Definition of a Linear Aircraft Model.* Scientific and Technical Information Division, National Aeronautics and Space Administration. August 1988. Reference Publication. NASA RP-1207.

3. **Graf, Richard K.** A Brief History of the HARP Project. *Astronautix.* [Online] [Cited: October 10, 2009.] http://www.astronautix.com/articles/abroject.htm.

4. **US Army Research Laboratory.** *NASA Orion Crew Exploration Vehicle - Pressure Telemetry Module (CEV-PTM) Free Flight Ballistic Range Experiment Performed at APG, MD on July 15, 2008.* Aberdeen : US Army, 2008.

5. **Etkin, Bernard.** *Dynamics of Atmospheric Flight.* Mineola, N.Y. : Dover Publications, Inc., 2005. 0-486-44522-4 (pbk.).

6. **Analog Devices.** ADXRS150 Single Chip Yaw Rate Gyro with Signal Conditioning. Norwood, MA : Analog Devices, Inc., 2004. Specification sheet for rate gyroscope.

7. **Tolson, Robert H.** *MAE 783: Space Flight Guidance and Navigation.* Raleigh : NC State University, Spring 2009.

8. *The variation of the specific heat ratio and the speed of sound in air with temperature, pressure, humidity, and CO2 concentration.* **Cramer, Owen.** 5, May 1993, Journal of the Acoustical Society of America, Vol. 93, pp. 2510-6.

Appendices

Appendix A: Derivation of transformation matrix from four state vectors utilizing triad method

To compute the DCM from the state vectors **a** and **b** in the body frame *b* and the inertial frame *n*, it is necessary to form a third reference frame *d*, called the triad frame. To construct this frame, define its first axis as the unit **b** vector:

$$\hat{\mathbf{d}}_1^b = \hat{\mathbf{b}}^b$$

$$\hat{\mathbf{d}}_1^n = \hat{\mathbf{b}}^n$$

where $\hat{\mathbf{b}}^b$ and $\hat{\mathbf{b}}^n$ are the unit vectors in the body and inertial frames, respectively. The second axis is then computed by including the similarly-normalized vector **a**:

$$\hat{\mathbf{d}}_2^b = \frac{\hat{\mathbf{b}}^b \times \hat{\mathbf{a}}^b}{\left|\hat{\mathbf{b}}^b \times \hat{\mathbf{a}}^b\right|}$$

$$\hat{\mathbf{d}}_2^n = \frac{\hat{\mathbf{b}}^n \times \hat{\mathbf{a}}^n}{\left|\hat{\mathbf{b}}^n \times \hat{\mathbf{a}}^n\right|}$$

The final axis of the triad frame is then the cross product of its first two axes:

$$\hat{\mathbf{d}}_3^b = \hat{\mathbf{d}}_1^b \times \hat{\mathbf{d}}_2^b$$

$$\hat{\mathbf{d}}_3^n = \hat{\mathbf{d}}_1^n \times \hat{\mathbf{d}}_2^n$$

Rotation matrices can now be formed between the body frame *b*, inertial frame *n*, and the triad frame *d*:

$$C_{db} = [\hat{\mathbf{d}}_1^b \quad \hat{\mathbf{d}}_2^b \quad \hat{\mathbf{d}}_3^b]$$

$$C_{dn} = [\hat{\mathbf{d}}_1^n \quad \hat{\mathbf{d}}_2^n \quad \hat{\mathbf{d}}_3^n]$$

where C_{db} is the DCM that transforms a vector from the body frame to the triad frame, and C_{dn} is the DCM that transforms a vector from the inertial frame to the triad frame. The DCM that transforms a vector from the body frame to the inertial frame is then

$$C_{nb} = C_{dn}^{\mathrm{T}} C_{db}$$

The transpose of the DCM is the rotation from the inertial frame to the body frame:

$$C_{bn} = C_{nb}^{\mathrm{T}}$$

This DCM can be used to transform any vector in the body or inertial frame to the other.

Appendix B: Computation of speed of sound and heat capacity ratio in humid air

A critical step in the process of recovery of flight parameters from pressure data is the method of computing the heat capacity ratio γ for humid air. For dry air, the calculation of these values is relatively straightforward, but more advanced models must be used when the relative humidity is significant. There have been a variety of models developed by over the years, each with an associated degree of accuracy within a certain temperature range. The equation describing specific heat ratio is

$$\gamma = c^2 \frac{\rho_\infty}{P_\infty}$$

where c is the speed of sound, ρ_∞ is the density of air, and P_∞ is the ambient pressure. The problem lies in computing the speed of sound and density for humid air. Finding these values involves the use of partial and saturation pressures (of which there are multiple ways to compute) and more elaborate models for the speed of sound than the classical $c_{dry\,air} = (331.3 + 0.606T_\infty)\,{}^{m}/_{S}$.

Instead, a model developed by Cramer (8) was utilized. It can be used to compute both speed of sound and specific heat ratio only by changing the coefficients. The model is described by the equation

$$\begin{aligned} f(T_\infty, P_\infty, x_w, x_c) &= a_0 + a_1 T_\infty + a_1 T_\infty^2 + (a_3 + a_4 T_\infty + a_5 T_\infty^2) x_w + (a_6 + a_7 T_\infty + a_8 T_\infty^2) P_\infty \\ &+ (a_9 + a_{10} T_\infty + a_{11} T_\infty^2) x_c + a_{12} x_w^2 + a_{13} P_\infty^2 + a_{14} x_c^2 + a_{15} x_w P_\infty x_c \end{aligned}$$

where T_∞ and P_∞ are the ambient temperature and pressure, respectively, and x_w and x_c are the water and carbon dioxide mole fractions, respectively. The values for an=1:15 are listed by Cramer, and have different values depending on if the computation is for speed of sound or for specific heat ratio. The model is valid under the following atmospheric conditions:

- Temperatures ranging from 0°C to 30°C
- Pressures from 75,000 Pa to 102,000 Pa

- H_20 mole fractions up to 0.06
- CO_2 concentrations up to 1%

Using this method, it is possible to compute the speed of sound and specific heat ratio for humid air using a single equation that is dependent only on temperature, pressure, and H_20 and CO_2 mole fractions.

Appendix C: Recovery of flight parameters from inertial measurement unit

To recover the orientation and trajectory in both the body and navigation systems, it is necessary to perform several transformations across the entire time range. Selecting an initial orientation, the quaternion history can be recovered by integrating the angular rates:

$$q = \int \dot{q}\, dt = \int \frac{1}{2}[q][\omega] dt$$

Where $[\omega] = [\omega_1 \quad \omega_2 \quad \omega_3 \quad 0]^T$ and

$$[q] = \begin{bmatrix} q_4 & -q_3 & q_2 & q_1 \\ q_3 & q_4 & -q_1 & q_2 \\ -q_2 & q_1 & q_4 & q_3 \\ -q_1 & -q_2 & -q_3 & q_4 \end{bmatrix}$$

Next, the acceleration of the center of mass of the vehicle is integrated to get the velocity in the range system:

$$\mathbf{v}^n = \int \ddot{\mathbf{r}}^n\, dt = \int (C_{bn}\mathbf{a}^b + \mathbf{g}^n)\, dt$$

where $\mathbf{g}^n = [0 \quad 0 \quad -g]^T$. As a check, the velocity computed here can be compared to the radar velocity, because they are both in the same coordinate system. The velocity in the body system must now be computed by applying the quaternion history to the velocity in the range system:

$$\mathbf{v}^b = C_{bn}\mathbf{v}^n$$

The velocity in the range coordinate system is then numerically integrated to get the position of the vehicle in the range system:

$$\mathbf{r}^n = \int \dot{\mathbf{r}}^n\, dt = \int \mathbf{v}^n\, dt$$

There are now histories for both position and velocity in the range and body systems, computed independently of any source external the IMU (such as radar). From here, the flight parameters can be computed. Mach number can be computed from the equation

$$M = \frac{|\mathbf{v}^b|}{c}$$